

**Department of Physics and Astronomy
Heidelberg University**

Bachelor Thesis in Physics
submitted by

Emilia Sedzielewski

born in Kaiserslautern (Germany)

2021

Iron spectroscopy in the VUV regime

This Bachelor Thesis has been carried out by Emilia Sedzielewski at the
Max-Planck-Institut für Kernphysik (MPIK) in Heidelberg
under the supervision of
Prof. Dr. José R. Crespo López-Urrutia

Abstract

In this work, iron ion spectra – especially of the charge state Fe V – were produced with the electron beam trap FLASH EBIT at the Max Planck Institut für Kernphysik (MPIK), and investigated with two different spectrometers which are sensitive in two different ranges of ultraviolet (UV) radiation. For this purpose, first the detector of the spectrometer which is sensitive in the vacuum ultraviolet (VUV) range was optimized so that it is now automatically moving into the respective focal position, to record focused and sharp spectra data.

A series of iron ion spectra were recorded at various electron beam energies, one of which at 2040 eV was discussed in detail. This was followed by an identification of several oxygen and carbon lines of charge states O III – O V and C III – C IV, as well as identification of desired iron lines of charge states Fe II, Fe III, and Fe V.

Zusammenfassung

In dieser Arbeit werden Eisenionen Spektren – besonders des Ladungszustands Fe V – mit der Elektronenstrahlfalle FLASH EBIT am Max-Planck Institut für Kernphysik (MPIK) produziert, und mit zwei verschiedenen Spektrometern, welche in zwei unterschiedlichen Bereichen ultravioletter (UV) Strahlung empfindlich sind, untersucht. Hierfür wurde zunächst Detektor der im Spektrometer welches im vakuumultavioletten (VUV) Bereich empfindlich ist so optimiert, sodass er nun automatisch in die richtige Position gefahren wird um fokussierte scharfe Spektren aufzunehmen, obwohl sich die Fokusposition aufgrund des verwendeten Messschemas stetig ändert.

Anschließend wurde eine Reihe von Eisenionenspektren bei verschiedenen Elektronenstrahlenergien aufgenommen, wovon eins bei 2040 eV ausführlich diskutiert wurde. Es folgte eine Identifikation von einigen Sauerstoff und Kohlenstofflinien der Ladungszustände O III – O V und C III – C IV, sowie eine vermutete Identifikation der gewünschten Eisenlinien der Ladungszustände Fe II, Fe III und Fe V.

Contents

1. Introduction and motivation	1
2. Theoretical background	5
2.1. Atomic structure	5
2.1.1. One-electron atom	5
2.1.2. Many-electron atoms	6
2.2. Electron Beam Ion Trap	10
2.2.1. Electrostatic potential	10
2.2.2. Electron beam	13
2.2.3. Electron impact ionisation	14
2.2.4. Electron impact excitation	14
2.2.5. Radiative recombination	15
2.2.6. Dielectronic recombination	16
3. Experimental setup	19
3.1. The FLASH EBIT	19
3.1.1. Electron gun	19
3.1.2. Magnet chamber	21
3.1.3. Collector	23
3.1.4. Vacuum and injection system	24
3.1.5. Magnetic structure	24
3.2. Spectrometers	25
3.2.1. 3m VUV grating spectrometer	25
3.2.2. EUV spectrometer	31
4. Focus optimisation of the ORFEUS detector	37
4.1. Measurement scheme	37
4.2. Interpolation of the motor focus positions	38

5. Iron Spectroscopy	41
5.1. DR measurement	41
5.2. Measurement scheme	41
5.3. Experimental parameters	43
5.4. Calibration	44
5.5. Spectra analysis	47
6. Summary and outlook	61
A. Appendix	67

1. Introduction and motivation

Man must rise above the Earth — to the top of the atmosphere and beyond — for only thus will he fully understand the world in which he lives.

- *Socrates, Philosopher*

Astronomy, utilized first by the ancient Greeks, represents the beginning of natural sciences as a whole and is still a major field of research today. Studying the night sky with its stars, galaxies and other celestial objects gives us insights into their chemistry and physics, shaping our understanding of nature. The knowledge gained through celestial observations is one of the building blocks of our view on the universe today [1].

The closest star to us and the center of our solar system, the sun, was the first that was studied extensively. To understand the nature of light and colours, Isaac Newton began a series of experiments with sunlight and glass prisms and made a groundbreaking discovery in the process [2]. He discovered that the white light emitted by the sun is in fact a superposition of light beams of different colors, which can be observed using the dispersive property of the prism, establishing our visible spectrum. The intensity distribution of the observed spectrum of the sun can be modelled by a black body spectrum. However, the actual spectrum deviates from the continuous black body spectrum in the form of distinct dark lines. These were first discovered by William Hyde Wollaston in 1802 [3] and were investigated further and documented by Joseph von Fraunhofer in 1814 [4]. Nearly half a century later, Gustav Kirchhoff and Robert Bunsen discovered a change in colour of a flame when burning chemical compounds, concluding it had to be characteristic to the burned substances [5]. They decided to refract the light of the coloured flame with glass prisms in order to investigate it and discovered that the emission lines of some of the analyzed elements matched the documented lines by Fraunhofer. Concluding the dark lines in the sun's spectrum originate due to absorption of light by elements in the outer sphere of the sun, they justified and established one of the most

important astrophysical methods, the spectrum analysis of stars. It is an irreplaceable technique to understand the formation and evolution of stars since the spectrum of an astronomical object provides information on its chemical composition, its temperature and its density.

Since the earth's atmosphere is opaque to ultraviolet (UV) and higher energetic radiation, only electromagnetic radiation in the visible, near infrared (NIR) and radio wave regime emitted by astronomical objects can be observed from earth. Therefore, space telescopes designed to carry out spectroscopic observations in the UV and X-Ray regime were launched. In the 1990s, the space telescope ORFEUS (Orbiting and Retrievable Far and Extreme Ultraviolet Spectrometer) flew aboard a Space Shuttle on two missions into space, acquiring several spectra in the far and extreme UV regime from over 200 interstellar objects [6][7]. Spectra of stars in several evolution stages were recorded, among others, of white dwarfs (WD).

All stars are formed from collapsing clouds and over the course of millions of years, these mass accumulating protostars settle down into a state of equilibrium, ignite hydrogen fusion and become what is known as a main-sequence star or dwarf star [8]. The main-sequence is a continuous band of stars that appears in a Hertzsprung-Russell diagram, which represents the relationship between the stars' absolute magnitudes or luminosities versus their stellar classifications or effective temperatures. The life of a star begins with the condensation and ignition, generating thermal energy in its dense core region through nuclear fusion of hydrogen into helium. The cores of main-sequence stars like our sun's are in hydrostatic equilibrium, where outward thermal pressure from the hot core is balanced by the inward pressure of gravitational collapse. Later, as the preponderance of atoms at the core becomes helium, stars like the sun begin to fuse hydrogen along a spherical shell surrounding the core, causing the star to gradually grow in size. Hence, it passes through the sub-giant stage until it reaches the red-giant phase. Stars with a similar mass like the sun can also generate energy through the fusion of helium at their core, where-as more massive stars can fuse heavier elements like neon originating from helium fusion into iron along a series of concentric shells. Once a star like the sun runs out of nuclear fuel, its core collapses into a white dwarf, representing the end point of its stellar evolution.

In general, most white dwarfs have a thin hydrogen shell, underneath a thicker helium shell, and its core consists of carbon and oxygen. Therefore, their atmospheres usually only show spectral lines of element from the upper two shells, classifying them as the spectral type DA for hydrogen, and as the spectral type DB for helium [9]. For many

years, this has been understood as an effect of gravitational separation in the very high gravitational fields in these objects [10]. All the more surprising is the observation, that at surface temperatures below 20 000 K some DA white dwarfs also show traces of heavier elements like iron, although the timescales for gravitational diffusion are short compared to evolutionary timescales. An example for an acquired spectrum with heavy metal lines is given by the high-resolution far-UV spectrum of the nearby DA white dwarf G191-B2B, recorded by the Hubble Space Telescope (HST). The spectrum contains several hundred absorption lines identified as Fe V and Ni V. These ions reside in the atmosphere of the white dwarf, and the observed features are formed in the outer layers near its surface.

The significance of these lines is given by a proposition of J.C. Berengut et al. in 2013 [11]. A new probe of the dependence of the fine structure constant α on a strong gravitational field using metal lines in the spectra of white dwarf stars was proposed. The fine structure constant is a fundamental physical constant which quantifies the strength of the electromagnetic interaction between charged particles. In [11] a variation of the fine structure constant $\Delta\alpha/\alpha$ could be determined by using the spectrum of DA WD G191-B2B and comparing it to laboratory spectra of the respective ions, showing the dependence of a fundamental constant on a strong gravitational field. This realisation justifies the need of Physics beyond the Standard Model, since the Standard Model does not intend a variation of the fine structure constant α , and is in general inconsistent with the theory of general relativity.

In this work, the goal is to acquire iron spectra, especially of the charge state Fe V, and to investigate them further. To produce these iron ions, the electron beam ion trap (EBIT) FLASH EBIT at the Max-Planck-Institut für Kernphysik (MPIK) is used. It is not only realizing the production, but also the simultaneous trapping and spectral analysis of ions [12]. EBITs can be tuned to a wide range of energies, meaning the spectral selectivity afforded by EBITs can be very high. These iron ions will be studied by recording their spectra with two spectrometers that are sensitive at different (UV) wavelength regimes. One of the spectrometers is equipped with the detector from the previous mentioned ORFEUS space telescope.

2. Theoretical background

For the understanding of the experiments on iron ions presented in this thesis, and the evaluation of the acquired spectra, it is essential to look into the fundamentals of atomic physics first. Therefore, some aspects of theoretical atomic physics relevant to this work are explained here [13].

2.1. Atomic structure

2.1.1. One-electron atom

The most simple bound atomic system is the one-electron (hydrogen) atom, which is why it is usually the starting point for atomic structure calculations. The hydrogen atom consists of a nucleus, which is a single proton with charge e and is surrounded by a single electron with charge $-e$. The opposite charge between the positive nucleus and negative electron results in the Coulomb potential that is given by

$$V(r) = -\frac{Ze^2}{(4\pi\epsilon_0)r}, \quad (2.1)$$

where $Z = 1$ describes the nuclear charge, ϵ_0 is the vacuum permittivity and r is the distance between both particles. Adding kinetic energy in the center-of-mass reference frame results in the formulation of the Hamiltonian

$$\hat{H} = -\frac{\hbar^2}{2\mu}\Delta_r + V(r). \quad (2.2)$$

The Hamilton operator \hat{H} depends on the potential $V(r)$ and the reduced mass $\mu = \frac{m_e M}{m_e + M}$, where m_e and M are the masses of the electron and nucleus, respectively. The reduced mass is used to reduce the two-body problem to a one-body problem. Due to the simple structure of the hydrogen atom, it is possible to calculate its wave functions

and energy eigenstates as exact solutions of the Schrödinger equation [14]:

$$\hat{H}\Psi(r, t) = i\hbar \frac{\partial}{\partial t} \Psi(r, t). \quad (2.3)$$

These solutions are non-relativistic approximations. By inserting the potential (2.1) into the Schrödinger equation, a differential equation is obtained that can be solved analytically is obtained. In fact, the hydrogen atom is the only atom for which the Schrödinger equation can be solved exactly. The wave function can be separated in variables into radial functions $R_{nl}(r)$ and spherical harmonics $Y_{ml}(\theta, \phi)$ [?]

$$\Psi(r, t) = R_{nl}(r) Y_{ml}(\theta, \phi). \quad (2.4)$$

Three parameters arise that are interpreted as the principal (n), azimuthal (l) and magnetic quantum number (m). The radial functions are

$$R_{nl}(r) = D_{nl} e^{-\frac{Zr}{na_0}} \left(\frac{2Zr}{na_0}\right)^l L_{n+l}^{2l+1} \left(\frac{2Zr}{na_0}\right) \quad (2.5)$$

where D_{nl} is a normalization constant, L_{n+l}^{2l+1} are the Laguerre polynomials and $a_0 = \frac{4\pi\epsilon_0\hbar^2}{m_e e^2}$ is the Bohr radius. The spherical harmonics are given by

$$Y_{ml}(r) = \sqrt{\frac{2l+1}{4\pi} \frac{(l-m)!}{(l+m)!}} P_{lm}(\cos\theta) e^{im\phi} \quad (2.6)$$

where $P_{lm}(\cos\theta)$ are the Legendre polynomials. To obtain the energy E of a state, the stationary Schrödinger equation needs to be solved (2.3)

$$\hat{H}\Psi(r, t) = E\Psi(r, t) \quad (2.7)$$

The energy values that solve the Schrödinger equation only depend on the choice for the principal quantum number:

$$E_n = -\frac{Z^2}{2n^2} \left(\frac{e^2}{4\pi\epsilon_0}\right)^2 \frac{\mu}{\hbar^2} \quad (2.8)$$

2.1.2. Many-electron atoms

After the one-electron atomic system, systems with several electrons should be considered next. Denoting that the Schrödinger equation has no exact solution for systems with N electrons, the following section will elucidate approximation methods that can be

used to obtain fairly accurate estimations in many cases. The problem with systems with several electrons is, that the electrons not only interact with the nucleus, but also with each other. In addition to mutual electrostatic and magnetic interactions between them, symmetry principles also have to be considered. The resulting Hamiltonian can be written as a sum over one-electron Hamiltonians plus an electron-interaction term

$$\hat{H}_{tot} = - \sum_i \left(\frac{\hbar^2}{2\mu} \Delta_{r_i} + V(\vec{r}_i) \right) + \sum_{j>i} \frac{e^2}{|\vec{r}_j - \vec{r}_i|} \quad (2.9)$$

Hartree method

The Hartree method is an iterative method of approximation for the determination of the wave function and energy levels of an electron for a many-electron system.

In this method, a single shell-electron i is considered first. Assuming a spherical potential $V^{(0)}(r)$ that takes into account the shielding of the rest of the shell electrons and inserting it into the Schrödinger equation (2.3), this leads to a wave function $\Psi_i^{(0)}(\vec{r}_i, t_i)$ for the regarded electron. Repeating this step leads to a series of assessed wave function $\Psi_i^{(0)}(\vec{r}_i, t_i)$ for every single electron of the system. Now, a new potential for every single shell electron can be calculated. For the single shell electron i with distance r_i from the nucleus, the wave functions of the remaining shell electrons $\Psi_j^{(0)}(\vec{r}_j, t_j)$ considering their mean charge distribution, are taken into account:

$$V_i^{(1)}(r_i) = -\frac{e}{4\pi\epsilon_0} \left[\frac{Z}{r_i} - \sum_{j \neq i} \int \frac{|\Psi_j^{(0)}(\vec{r}_j, t_j)|^2}{r_{ij}} dt_j \right] \quad (2.10)$$

By inserting this potential for the next electron i , a new set of wave functions $\Psi_i^{(1)}(\vec{r}_i, t_i)$ results. Using these resulting wave functions, a new potential for every shell electron i can be calculated. This procedure is now repeated until the inserted potential leads to converged wave functions which reproduce this potential within certain error limits.

As mentioned before, the total wave function of the system is composed of the single electron wave functions. Since the system consists of more than one electron which is a fermion, the total wave function always has to be antisymmetric with respect to the exchange of any two electrons. This general symmetry rule is also called the Pauli principle. (demtröder 2018). This principle can be enforced by setting up the Slater

determinant

$$\Psi_{tot}(\vec{r}_1, \vec{r}_2, \dots, \vec{r}_N) = C \begin{vmatrix} \Psi_1(\vec{r}_1) & \Psi_1(\vec{r}_2) & \cdots & \Psi_1(\vec{r}_N) \\ \Psi_2(\vec{r}_1) & \Psi_2(\vec{r}_2) & \cdots & \Psi_2(\vec{r}_N) \\ \vdots & \vdots & \vdots & \vdots \\ \Psi_N(\vec{r}_1) & \Psi_N(\vec{r}_2) & \cdots & \Psi_N(\vec{r}_N) \end{vmatrix} \quad (2.11)$$

where C is a normalisation constant. By solving the stationary Schrödinger equation, the energy of the system is determined.

Hartree-Fock method

So far, the spin of the electron has not been considered. In the Hartree-Fock method, however, the spin of the electrons is taken into account. In general, each electron wave function can be written as a product of the spatial component $\Phi(\vec{r})$ and spin component $\chi(\vec{s})$, and in the section above only the spatial component was regarded:

$$\Psi(\vec{r}, \vec{s}) = \Phi(\vec{r})\chi(\vec{s}) \quad (2.12)$$

By taking the spin component into account, significantly more accurate results are obtained. Except for this splitting of the wave functions, this method follows the same steps as the Hartree method. To obtain even more accurate results, relativistic effects must be taken into account. Then, instead of the Hamilton operator from equation (2.9), the relativistic Dirac-Coulomb-Breit Hamiltonian is used, which unites a total number of six operators. Most importantly, it combines the non-relativistic Hamiltonian with the dependence of mass on velocity and the spin-spin interaction. By following the same procedure as in the methods before with the new operator, the resulting method is called the Dirac-Coulomb-Breit method.

Configuration Interaction (CI)

An even better method than the Hartree-Fock method to include the interactions between electrons in a multi-electron system, is Configuration Interaction[15]. For this purpose, the wave function is built up from more than one electron configuration, in the form of a linear combination of Slater determinants. Based on the wave functions we derived before with the Hartree-Fock method, it belongs to the post-Hartree-Fock methods. The total wave function therefore is given by the sum of Slater determinants

Ψ_k :

$$\Psi_{CI}(\vec{r}, \vec{s}) = \sum_k c_k \Psi_k \quad (2.13)$$

Each determinant Ψ_k stands for a specific system configuration, meaning a certain distribution of the electrons on the possible energy levels. These configurations are weighted by the factors c_k , which are determined by diagonalizing the total Hamilton operator (2.9). By using the stationary Schrödinger equation (2.3) to determine the energy of the system, this results in new energy contributions due to the interaction of the single configurations. These energy contributions lead to an even more accurate result for the energy of the system. Logically, the more configurations Ψ_k are considered the more accurate the end result becomes. If every configuration was considered, this would even lead to an exact solution. But because the dimensions of the Hamilton matrix scale exponentially for solving eigenwert problems of a system, the accuracy is limited by the given computing power. Therefore, due to the long CPU time and large memory required for CI calculations, this method is limited to relatively small systems.

2.2. Electron Beam Ion Trap

The ions studied in this work were produced and trapped in the electron beam ion trap (EBIT) FLASH EBIT at the Max-Planck-Institut für Kernphysik (MPIK) in Heidelberg. In an EBIT ions are generated and trapped using a magnetically focused electron beam and a positive trapping potential that is tuned by trap electrodes. A more detailed and comprehensive discussion on the utilized FLASH EBIT is given in chapter 3.2.

In this section, the electrostatic potential in the trap and the most significant processes taking place in an EBIT are introduced and given theoretical background. The processes can be divided into two categories: ion-electron and ion-ion interactions. The first ones are responsible for the ionization and recombination of ions, while the second lead to charge exchanges and thermalization due to collisions. However, the electron density and relative kinetic energy favours ion-electron interactions in the interaction region, therefore only these are described further.

2.2.1. Electrostatic potential

To evaluate recorded measurements, it is essential to know the exact energy of the electron beam in the trap center [16]. Generally, the electrostatic potential in which the ions are located has two origins. On the one hand, it depends on the voltages applied to the trap electrodes which create a potential well to trap ions. On the other hand, it depends on the superposition of the negative space charge generated by the electron beam, somewhat reduced by the positive space charge generated by the trapped ions. By using Gauss's law, the contribution of the space charge potential Φ of the electron beam can be determined

$$\Phi_e = \oint_A \vec{E} \cdot d\vec{A} = \frac{Q}{\epsilon_0}, \quad (2.14)$$

where Q is the charge of the electrons and ϵ_0 is the permittivity of free space. Approximating the electron beam as an infinitely elongated cylindrical charge distribution of constant charge density with the radius r_H , this results in the local charge density

$$\rho_e = \frac{I_e}{\pi r_H^2 v}, \quad (2.15)$$

with I_e being the electron beam current and v representing the longitudinal velocity of the electrons.

Now, two cases have to be considered, depending on the distance r to the beam center:

(a) $r > r_H$:

$$\oint_A \vec{E} \cdot d\vec{A} = \frac{Q}{\epsilon_0} \quad \text{with } Q = \pi r_H^2 \rho l$$

$$\Rightarrow 2\pi r l E(r) = \frac{\pi r_H^2 \rho l}{\epsilon_0}$$

$$\Leftrightarrow E(r) = \frac{r_H^2 \rho}{2r \epsilon_0} \quad \text{with (2.15)}$$

$$= \frac{I_e}{2\pi v \epsilon_0} \frac{1}{r}$$

$$\Rightarrow \Phi_e = \int_0^r E(r') dr' = \frac{I_e}{2\pi v \epsilon_0} \ln(r).$$

Defining the constant Φ_0 as

$$\Phi_0 = \frac{I_e}{2\pi v \epsilon_0} \quad (2.16)$$

and considering the boundary condition of a well-defined potential Φ_D at the surface of the drift tube with inner radius r_D , this leads to the following expression for the space charge potential

$$\Rightarrow \Phi_e = \Phi_D + \Phi_0 \ln\left(\frac{r}{r_D}\right). \quad (2.17)$$

The second case that is to be considered is:

(b) $r \leq r_H$:

$$\oint_A \vec{E} \cdot d\vec{A} = \frac{Q}{\epsilon_0} \quad \text{with } Q = \pi r_H^2 \rho l$$

$$\Rightarrow 2\pi r l E(r) = \frac{\pi r^2 \rho l}{\epsilon_0}$$

$$\begin{aligned} \Leftrightarrow E(r) &= \frac{r\rho}{2\epsilon_0} && \text{with (2.15)} \\ &= \frac{I_e}{4\pi v \epsilon_0 r_H^2} r \end{aligned}$$

$$\Rightarrow \Phi_e = \int_0^r E(r') dr' = \frac{1}{2r_H^2} \Phi_0 r^2.$$

Using (2.17) the result is

$$\Phi_e = \Phi_D + \frac{1}{2} \Phi_0 \left[\left(\frac{r}{r_H} \right)^2 + 2 \ln \left(\frac{r_H}{r_D} \right) - 1 \right]. \quad (2.18)$$

Therefore, the complete expression for the space charge potential for all $r \in [0; r_D]$ is

$$\Phi_e = \begin{cases} \Phi_D + \frac{1}{2} \Phi_0 \left[\left(\frac{r}{r_H} \right)^2 + 2 \ln \left(\frac{r_H}{r_D} \right) - 1 \right] & r \leq r_H \\ \Phi_D + \Phi_0 \ln \left(\frac{r}{r_D} \right) & r > r_H \end{cases}. \quad (2.19)$$

The potential scales linearly with the beam current I , which is an important insight for evaluating the measurements later on.

The total acceleration potential traversed by an electron emitted from the surface of the cathode, at a potential Φ_C , arriving in the center of the trap is given by

$$U_{kin} = \Phi_D - \Phi_C + \Phi_0 \ln \left(\frac{r_H}{r_D} \right) + \Phi_I + \Phi_A \quad (2.20)$$

along the symmetry axis along the beam for $r = 0$. Here, Φ_I is the positive space charge potential of the ions and Φ_A is a potential which is a composition of material-dependant properties. As a conclusion, a higher electron beam space-charge potential reduces the total kinetic energy of the electrons.

2.2.2. Electron beam

As derived above, the space charge potential is dependant on the distance to the beam center. Therefore, the energies of the different electrons that have different distances to the beam center are not affected by the space charge potential by the same scale. This results in a beam energy that is not sharply defined. Since the ions are not always located in the very center of the beam, they do not interact with electrons of a perfectly well-defined energy. This is the major factor that limits the resolution of the experiment. One way to tackle the problem, is to tune the beam current as low as possible. The space charge potential scales linearly with the beam current, therefore a smaller current would lead to a smaller variation of space charge potential, and therefore to a better resolution. But this would lead to one problem. The reaction rate in the trap scales quadratically with the beam current [17]:

$$R \propto I_e^2. \quad (2.21)$$

Therefore, it has to be considered how small the beam current can be tuned until the reaction rate in the trap becomes too low.

Another possibility to improve the resolution would be to lower the temperature of the ions in the trap. Thinking of the ion cloud as an ideal gas, and defining T_{ion} as the temperature of the ions, the average kinetic energy of the ions is:

$$\overline{E_{kin}} = \frac{3}{2} k_B T_{ion}, \quad (2.22)$$

where k_B represents the Boltzmann constant [18]. From this, and with 2.19, the maximum distance from the beam center for an ion with charge q can easily be derived

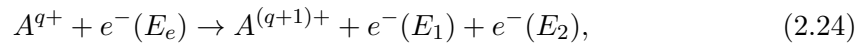
$$r_{max} = \begin{cases} r_H \sqrt{\frac{6k_B T_{ion} \pi v_e \epsilon_0}{I_e q} - 2 \ln\left(\frac{r_H}{r_D}\right)} & r \leq r_H \\ r_D \exp\left\{\frac{3k_B T_{ion} \pi v_e \epsilon_0}{I_e q}\right\} & r > r_H \end{cases}. \quad (2.23)$$

If the radial expansion of the ion cloud is small, interactions only take place near the beam center, which leads to a limitation of the electron energies contributing to interactions. This only applies for low temperatures, since the radial expansion scales significantly with the temperature. By flattening the trap in axial direction the ions with the highest energy escape the trap, which results in the temperature sinking and the radius shrinking. This method is called evaporative cooling [19]. As in the first solution approach, the reaction rate is also reduced for flatter trap potentials. Therefore, it is again to consider

to what extent this method can be used. In practice, both methods are combined, with the goal of reaching a sufficiently high reaction rate.

2.2.3. Electron impact ionisation

In order to be able to investigate ions in the trap, neutral gas is injected into the EBIT, which is then ionized by an electron beam. This process is called electron-impact ionisation (EII). Here, an electron with sufficiently high energy collides with an atom or ion and transfers its kinetic energy to its collision partner, which expels a shell electron. The process is described by



where the incoming electron has the kinetic energy E_e in the COM system an ion A with charge q [19]. E_1 and E_2 represent the energies of the two electrons after the collision. Since energy is conserved, the sum of the energies of the free electrons is equal to the difference between the energy of the incoming electron and the ionization potential I_P of the least-bound electron

$$E_1 + E_2 = E_e - I_P \stackrel{!}{\geq} 0 \quad (2.25)$$

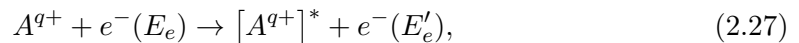
The cross section $\sigma_{q \rightarrow q+1}^{\text{EII}}$ for this process is given by the semi-empirical Lotz formula, and it depends mainly on E_e and the ionization potential I_{P_i} of the i th subshell [20]

$$\sigma_{q \rightarrow q+1}^{\text{EII}} \approx \sum_{n=1}^N a_i q_i \frac{\ln(\frac{E_e}{I_{P_i}})}{E_e I_{P_i}} \left(1 - b_i \exp \left\{ c_i \left(-\frac{E_e}{I_{P_i}} - 1 \right) \right\} \right). \quad (2.26)$$

with a_i , b_i and c_i being constants that depend on the respective element and need to be determined by other means. q_i is the number of equivalent electrons in the same subshell.

2.2.4. Electron impact excitation

A simple way of exciting the ion is a free electron interacting with an ion A without being captured. This process is called electron-impact excitation (EIE).



resulting in an increase of the ions energy and a reduction of the kinetic energy of the free electron

$$\Delta E_{A^q} = \Delta E_e = E_e - E'_e. \quad (2.28)$$

The cross section $\sigma_{i \rightarrow j}^{\text{EIE}}$ for a transition from energy level i to j of an ion can be approximated by the van Regemorter formula [21]

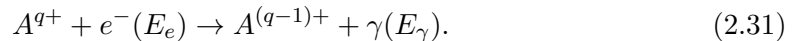
$$\sigma_{i \rightarrow j}^{\text{EIE}} = \pi a_0^2 \frac{8\pi f_{ij}}{\sqrt{3}} \frac{R_y^2}{E_{ij}^2} \frac{G(x)}{x}, \quad (2.29)$$

where the dimensionless parameter x is defined as the ratio between the kinetic energy of the incoming electron and the threshold energy E_{ij} : $x = E_e/E_{ij}$. f_{ij} is the oscillator strength between the two energy levels, R_y is the Rydberg energy and $G(x)$ is the effective Gaunt factor. $G(x)$ scales the classical oscillator strength to that of a quantum mechanical system, and can be approximated as

$$G(x) = 0.349 \ln(x) + 0.455 x^{-1} + 0.0988. \quad (2.30)$$

2.2.5. Radiative recombination

Another possible outcome of an ion-electron interaction is radiative recombination (RR). In this case, the ion captures a free electron, lowering its own charge state by one, and emits a photon γ of the energy E_γ



After the recombination, the electron experiences the binding energy I_P , which, added to the kinetic energy of the projectile, has to equal the photon energy due to energy conservation,

$$E_e + I_P = E_\gamma = \hbar\omega_{RR}, \quad (2.32)$$

where \hbar is the reduced Planck constant and ω is the angular frequency of the emitted photon. RR is the time-reversed process of photo-ionization, and is illustrated in Fig.

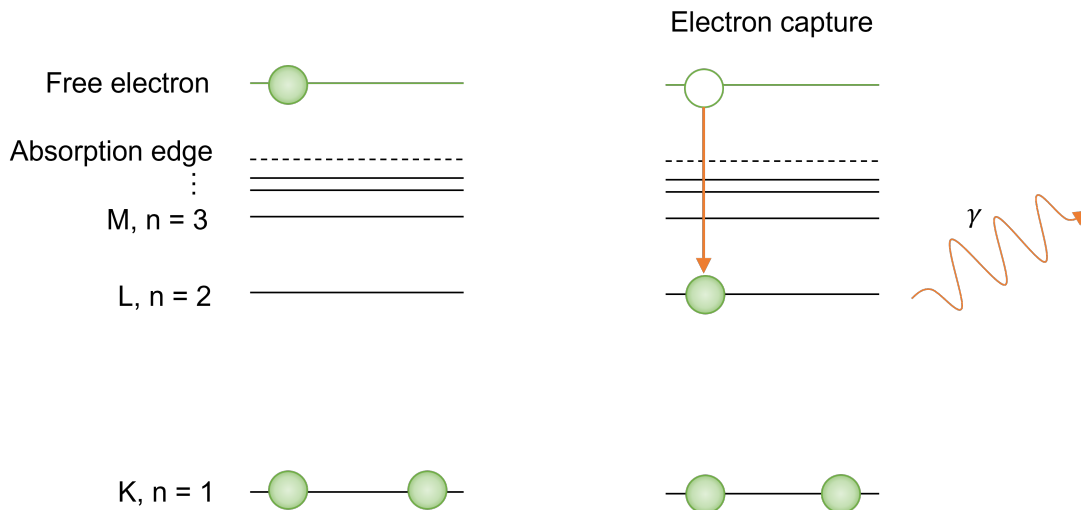


Figure 2.1.: Schematic diagram of radiative recombination. This example shows both states in the K shell initially occupied and a free electron is captured into the L shell.

2.1. As explained further by Kim and Pratt [22], the RR cross section is estimated as

$$\sigma^{\text{RR}} = \frac{8\pi\alpha^3 Z_{\text{eff}}^4}{\sqrt{27}n^3 E_e E_\gamma} \quad (2.33)$$

where n is the principle quantum number of the energy level in which the electron is located after the capture. The quantity Z_{eff} is the effective proton number, which is smaller than the proton number Z due to partial shielding by the electron shell. α is the fine structure constant of the electromagnetic interaction.

2.2.6. Dielectronic recombination

In contrast to RR, in dielectronic recombination (DR) the capture of an electron does not directly result in the emission of a photon, but leads to an excitation of another bound electron. This is a two-step process: first, a free electron is captured into a vacant excited state of the ion A^{q+} , while a core electron with energy E_1 is simultaneously promoted to a higher-lying excited state with energy E_2 , forming an intermediate (singly, doubly or multiply) excited state. This is then followed in the second step by a de-excitation under the emission of a photon (or several photons). The whole process is illustrated in

Fig. 2.2 and can be written as:

$$A^{q+} + e^{-} \rightarrow [A^{(q-1)+}]^* \rightarrow [A^{(q-1)+}] + \hbar\omega_{DR}. \quad (2.34)$$

This process is resonant and can only happen, if the kinetic energy of the free electron plus the potential energy it has after being captured, equals the excitation energy. This resonance condition is written as

$$\Delta E = E_2 - E_1 = E_e + I_P. \quad (2.35)$$

For this work, one specific kind of DR process is of special interest as it is going to be measured later. Here, a free electron is captured into the L shell, leading to an excitation of a K-shell electron into the L shell. For a helium-like initial state and the final excited state $1s2l2l'$ (l, l' being single-electron angular momentum states), the intermediate excited state decaying process can be written as:

$$\begin{aligned} A^{(Z-2)+} + e^{-} (1s^2) &\rightarrow [A^{(Z-3)+}]^* (1s2l2l') \\ &\rightarrow A^{(Z-3)+} (1s^22l \text{ or } 1s^22l') + \hbar\omega(K_\alpha). \end{aligned} \quad (2.36)$$

This process is called KLL DR and is illustrated in Fig. 2.2. Alternatively, in the second step the ion may as well return to its initial state. For this purpose the formed excited state $[A^{(q-1)+}]^*$ decays to the ground state via an Auger auto-ionization process, leading again to a change in charge $A^{(q-1)+} \rightarrow A^{q+}$ [19]. However, radiative de-excitation via emission of photons strongly dominates. The cross section $\sigma_{i \rightarrow d \rightarrow f}^{\text{DR}}(E)$ states the probability for electronic capture from an initial state i , under excitation of an intermediate (often doubly-excited) state d , to a final state f and is given by [19]

$$\sigma_{i \rightarrow d \rightarrow f}^{\text{DR}}(E) = \frac{2\pi^2 \hbar^4 A_r^{d \rightarrow f}}{p^2 \Gamma_d} L_d(E) V_{DC}^{i \rightarrow d}, \quad (2.37)$$

where $p = \sqrt{(E/c)^2 - m^2 c^2}$ is the momentum of the projectile electron with the kinetic energy E . The dependence on the energy is described by the Lorentzian profile

$$L_d(E) = \frac{\Gamma_d / (2\pi)}{(E_i + E - E_d)^2 + \frac{\Gamma_d^2}{4}}, \quad (2.38)$$

with Γ_d being the natural width of the intermediate state. Said quantity is resulting from both radiative and auto-ionization decay channels: $\Gamma_d = \hbar(A_r^d + A_a^d)$. The dielectronic

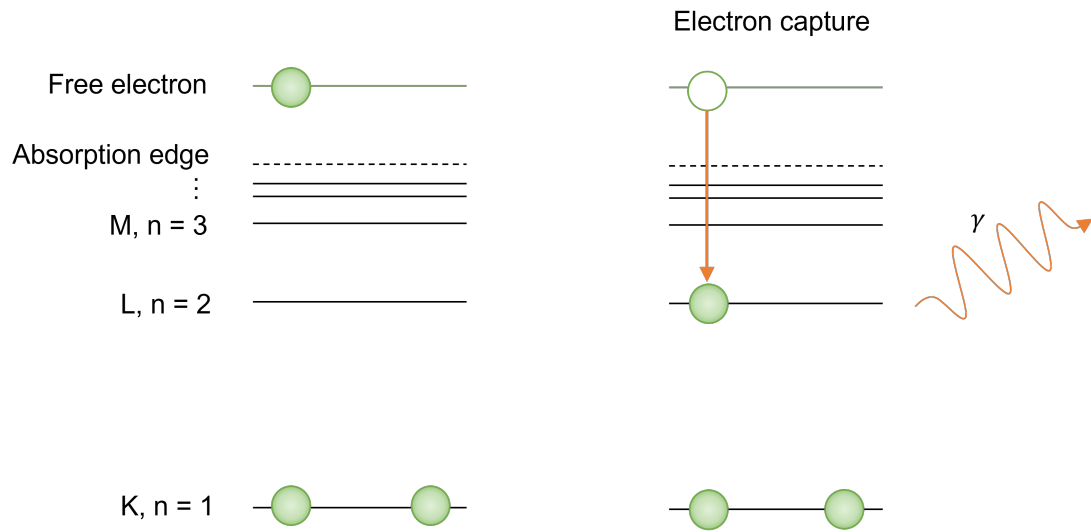


Figure 2.2.: Schematic diagram of KLL dielectronic recombination. In this example, a free electron is captured into the L shell under excitation of a K-shell electron into the L shell. Next, one of the L shell electrons is de-excited to the ground state under emission of a photon.

capture rate V_{DC} and the Auger process rate are connected:

$$V_{DC}^{i \rightarrow d} = \frac{2J_d + 1}{2(2J_i + 1)} A_a^{d \rightarrow i}, \quad (2.39)$$

where the J_d and J_i are the respective total angular momenta of the intermediate/initial state.

3. Experimental setup

The experimental setup for the investigation of iron ion spectra, conceptually consists of two parts, as described in Chapter 1. The first part is the instrument that is used to generate the ions that can be utilized for spectroscopy, the FLASH EBIT at the MPIK in Heidelberg. By tuning the electron beam, it is possible to configure different distributions of charge states of ions, which are then captured in a potential well. Those trapped ions can be investigated with the second part of the setup, which is made up of spectrometers. This chapter deals with the structure and operating principles of both parts.

3.1. The FLASH EBIT

Every EBIT can be divided into three main parts: the electron gun, the magnet chamber and the collector (see Fig. 3.1). The electron gun provides free electrons with the help of a heated cathode, which are accelerated towards the magnet chamber. The magnet chamber is surrounded by a pair of superconducting Helmholtz coils which generate a strong magnetic field to focus the electron beam. Also, it features nine electrodes that form the ion trap, which are called drift tubes. The collector captures the electron beam after it has passed the trap region. The atoms that are to be ionized and trapped, are inserted into the EBIT by a gas injection system. In the trap center, the ions are trapped axially by the electrostatic potential of the drift tubes, and radially by the space charge of the electron beam.

3.1.1. Electron gun

In the electron gun, the electrons are set free by a thermionic dispenser cathode, which consists of a barium-permeated tungsten matrix. To obtain an electron beam that is as focused as possible, the temperature of the freed electrons has to be kept as low as possible. By electrical heating to high temperatures of up to 1000 K, electrons are released from the barium. Close to the thermionic dispenser cathode a focus electrode

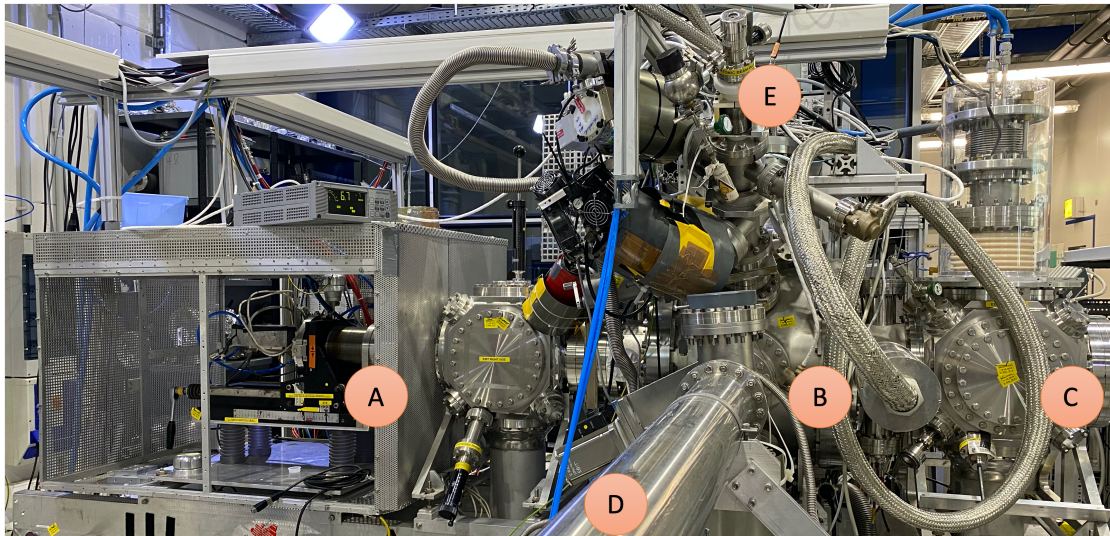


Figure 3.1.: A photograph of the FLASH EBIT. The electron beam is produced in the electron gun (A) and passes the magnet chamber (B) where it ionizes ions which injected by the needle valve (E) into the trap. Afterwards, it is absorbed by the collector (C). The produced ions can be investigated with the VUV spectrometer (D).

is located (see Fig. 3.2, which accelerates the freed electrons. By adjusting its potential, the current of the electron beam is set. If the potential was set strongly negative, the beam would be shut down due to repulsion. Next in the line is the anode. Like the focus electrode, it can be used to accelerate the electrons in the directions of the trap. Practical experience has shown, that the use of the focus electrode provides a more focused beam [23]. Therefore, the adjustment of the anode is optional and is in practice only used, if very high total beam energies in the range of several keV are striven for.

The electron gun is surrounded by two magnetic coils, the bucking and the trim coil. The bucking coil used to compensate the strong magnetic field that is generated by the superconducting Helmholtz coils around the magnet chamber. This is due to the diameter of the electron beam being smaller, if it is constituted in the absence of a magnetic field, compared to the case where a magnetic field is present [24]. The function of the trim coil is the vernier adjustment of the beam position.

To withstand the high temperatures of the thermionic cathode, the electron gun is water cooled. To ensure that the electron beam crosses the trap region as central as possible, the position of the electron gun can be adjusted along x- y- and z- direction. Additionally, the electron gun has its own set of vacuum pumps and can therefore be decoupled from the rest of the EBIT by closing a valve, in case of any necessary main-

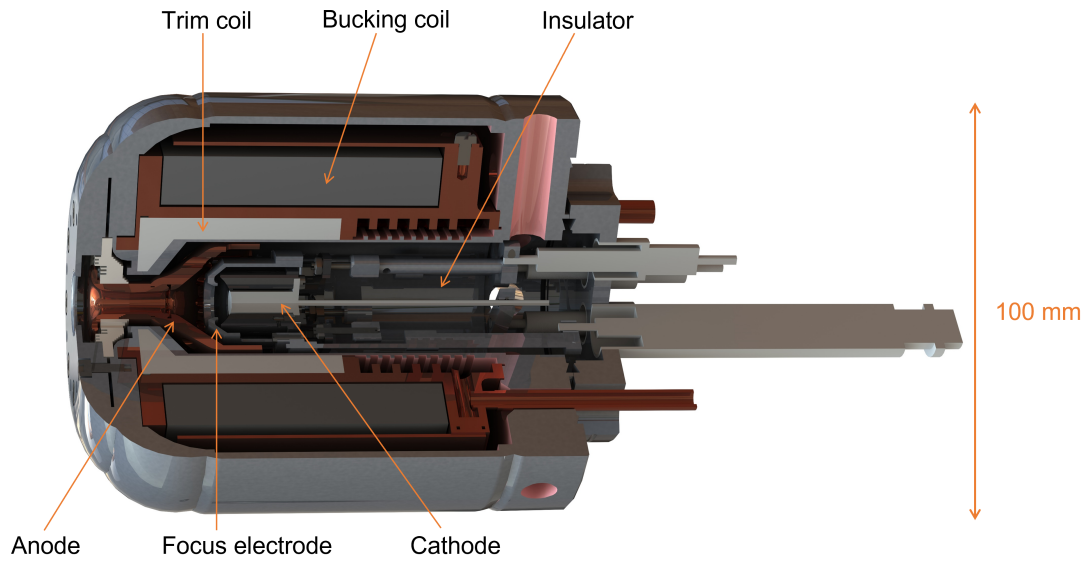


Figure 3.2.: Schematic depiction of the electron gun and its components.

tenance work.

3.1.2. Magnet chamber

The core piece of the EBIT is constituted by the drift tubes in the magnet chamber. By adjusting the applied voltages, they are responsible for trapping the ions with a potential well. A total number of nine copper drift tubes are integrated in the trap. The forms of the inner seven drift tubes are hollow cylinders, the diameters increase conically from the trap center outwards. The remaining two outermost drift tubes have a shape somewhat resembling a trumpet, whose openings facing the electron gun and the collector respectively. The benefit of this trumpet-like form is, that the trap center is isolated from thermal radiation from the warmer parts of the EBIT [16]. The drift tube arrangement can be seen in Fig. 3.3.

The electrodes are separated by sapphire insulators. This specific material was chosen, because sapphire has the property of being an excellent heat conductor at very low temperatures while still being an electrical insulator [25]. When the radiation of the ions inside the trap hits the electrodes, the transferred heat can be transported away. This way, the electrodes are kept from heating up. Moreover, the whole drift tube group is connected to a cryocooler, which is a refrigerator designed to reach cryogenic temperatures by using liquid helium.

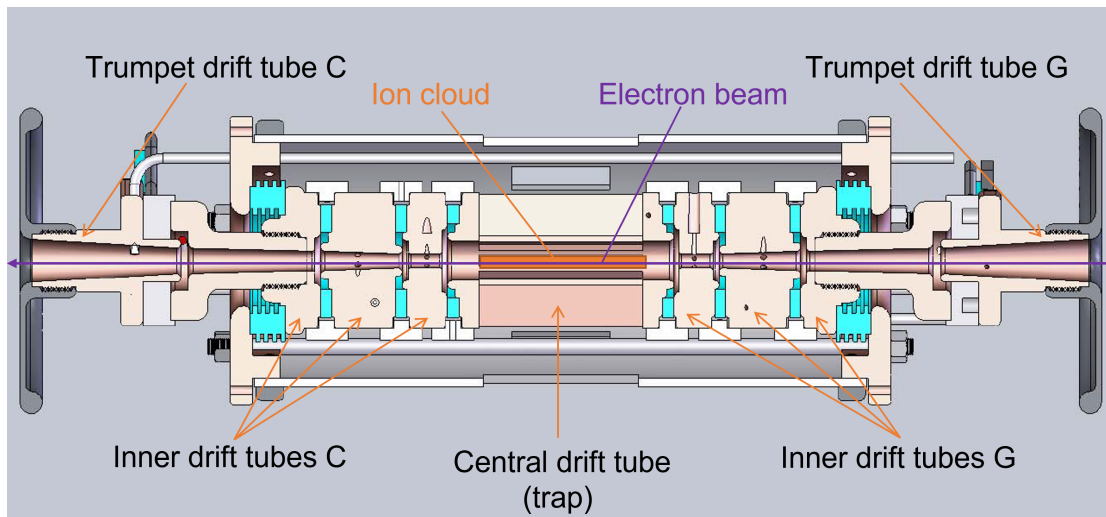


Figure 3.3.: Schematic depiction of the nine drift tubes.

The central drift tube is the biggest out of the nine and has several openings in its cylinder surface to allow lines of sight from the trap center to the detectors. All the drift tube potentials are offset by a common bias voltage, and the difference to the cathode voltage is responsible for the acceleration of the electrons.

Moreover, the voltages of the drift tubes can be adjusted separately to trap the ions in the direction of the electron beam. To obtain this in practice, the two electrodes around the central one are set to the highest potential. The following electrode's potentials are declining the further away they are located from the trap center. The innermost electrode is mostly set to a slightly lower potential than its two neighbouring electrodes, to form a potential well. But in general, it is also possible to set this electrode on the overall highest potential and still capture ions. The trap is then still working due to the space charge of the electrons. This mode of operation works especially well for heavier ions. By setting the innermost electrode onto a very high potential, the trap discards of any unwanted ions. For instance barium ions, which find their way into the trap centre from the barium-permeated thermionic dispenser cathode. Therefore, it is recommended to use a 'dump' where once every few seconds the potential of the innermost electrode sets to a very high value for a short amount of time.

The trap region is equipped with windows, so that the radiation that arises by the collision of ions and electrons can be decoupled. At this stage, different devices can be used to detect and analyze the radiation. For the measurements carried out in this work, two spectrometers were used: one VUV (vacuum ultraviolet) and one EUV (extreme

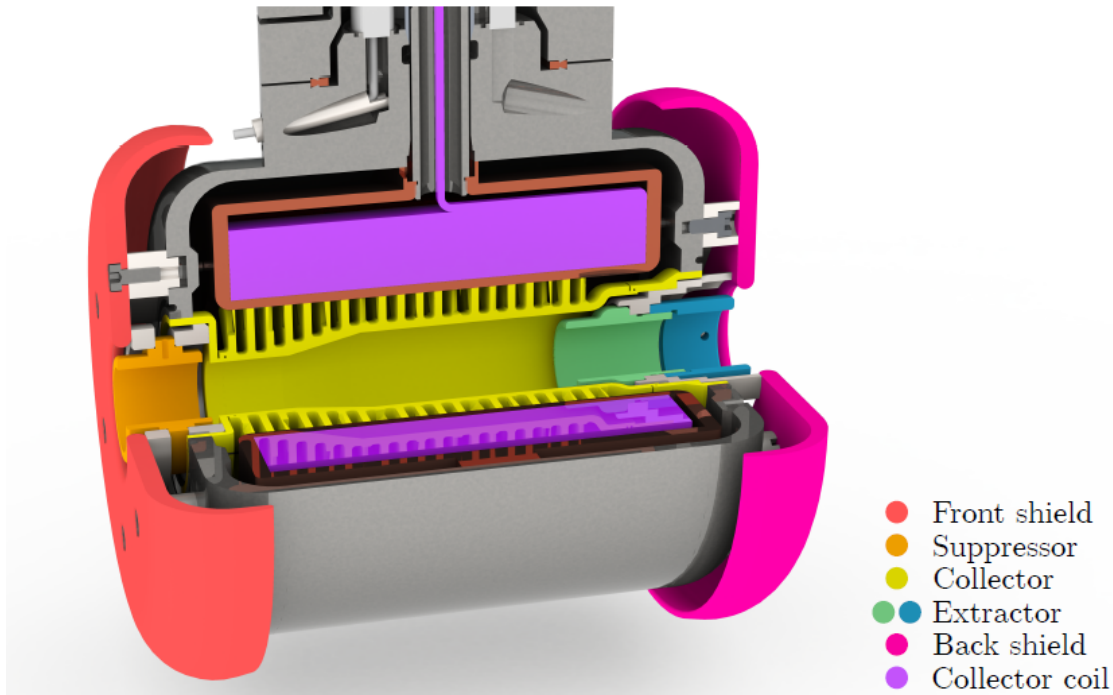


Figure 3.4.: Schematic depiction of the collector and its components, taken from [26].

ultraviolet) spectrometer.

3.1.3. Collector

After the electron beam has passed the trap region, it starts to get decelerated by the electric field that is constituted by the drift tubes, before it reaches the collector and gets absorbed. The collector consists of three different electrodes: a suppressor electrode, a hollow water-cooled copper electrode and an extractor electrode. The detailed setup of the collector can be seen in Fig 3.4.

First, the electron beam passes the suppressor and enters the hollow electrode. The suppressor lies on a slightly more negative potential to prevent secondary electrons, that are set free when primary electrons hit the electrode, from exiting the collector. The extractor, which is located on the opposite site of the collector, is set to a negative potential, which stops electrons from leaving the detector. The copper electrode is surrounded by a magnetic coil, which eliminates the remnants of the magnetic field from the superconducting magnet. Without a magnetic field, the electron beam diverges and hits the copper electrode broadly [24].

3.1.4. Vacuum and injection system

The vacuum inside the EBIT is generated and maintained by a two-stage pumping system. Therefore, the magnet chamber, the electron gun chamber as well as the collector chamber are equipped with turbomolecular pumps.

As explained in Chapter 1, the ions of interest in this work are iron ions. To produce these ions, iron is inserted into the EBIT by a gas injection system, which consists of a needle valve that is attached to a gas source. Since iron on its own is solid at room temperature, iron pentacarbonyl ($\text{Fe}(\text{CO})_5$) is used. A chemical compound that is liquid at room temperature, but has a vapour pressure of 30 mbar. Therefore, enough molecules are in the vaporized state inside the bottle that is attached to the injection system, such that a sufficient amount of iron molecules reaches the trap. There, the molecules are ‘broken up’ by the electron beam and iron atoms and lowly charged ions are set free. By regulating the electron beam energy, the distribution of the iron ions can be adjusted as necessary. Furthermore, there are two differential pressure levels at the injection system, maintained by two turbomolecular pumps that are connected to the EBIT by a valve. This two-stage pumping system allows a precisely controlled gas flow into the trap chamber, while maintaining the ultra-high vacuum.

3.1.5. Magnetic structure

The magnetic structure produces a magnetic field that condenses the electron beam to achieve high current densities [24]. At the FLASH EBIT a pair of superconducting Helmholtz coils is used to generate a magnetic field with a strength of up to 6 T. They are located around the trap area, where the coils have a bigger distance than they usually would have in a Helmholtz configuration. This way, a nearly constant magnetic field in the center of the trap is generated but there is also plenty of space between the coils that can be reached with the injection system and detectors. This is a big advantage of the Helmholtz coils compared to one single, long magnetic coil. The magnet is kept nearly steady at a temperature of 4 K by using a cryocooler. A series of thermal shields are setup around this area to isolate the magnetic chamber and prevent radiative heating.

3.2. Spectrometers

As mentioned in Chapter 1, the measurements were taken with two different spectrometers which are sensitive in different ranges of the ultraviolet (UV) regime. Conceptually, the term vacuum ultraviolet (VUV) is defined as the range from 10 nm to 200 nm and extreme ultraviolet (EUV) as 10 nm to 121 nm, and the expected lines from this work fall into the intersection. The first spectrometer that is utilized is the 3m VUV grating spectrometer, which has an arm length of 3m, as the name suggests, and is most sensitive in the range of ~ 30 -150 nm. This device is used to record wide-range spectra of the interesting charge states of ions. The second spectrometer is the EUV spectrometer, which is a more compact setup, covering a wavelength range from ~ 5 -30 nm.

3.2.1. 3m VUV grating spectrometer

As already indicated by the expression ‘vacuum ultraviolet’, this regime of radiation is absorbed by air, and therefore, the whole experimental setup must be located inside a vacuum chamber to minimize distortions. In comparison to the visible regime, the VUV regime presents a challenge when it comes to designing optics, as there are no lenses available, and the normal reflectivity with less than 30 % is rather low. Therefore, grazing incidence is in general a good solution, as it provides higher reflectivity even for small angles. Also, the grating has a concave curvature radius R , hence the grating has not only dispersive properties, but is also able to focus the outgoing rays. A simple but effective reflective spectrometer design was published by Rowland [27].

Rowland circle

An illustration of the concept can be seen in Fig. 3.5. The utilized concave reflective grating with curvature of radius R , has the focal length $R/2$. Drawing the grating surface normal and marking the distance which equals the focal length $R/2$, the center of the so-called Rowland circle can be drawn. It lies tangentially to the grating and its diameter equals the curvature radius R . This has the simple advantage, that if a point-like light source is located on the Rowland circle, then the light gets reflected and focused onto another point that is located on this circle. Using the grating equation, the angle of reflection ϕ_n for a spectral mode and wavelength can be calculated

$$n \cdot \lambda = g \cdot (\sin(\phi) + \sin(\phi_n)), \quad (3.1)$$

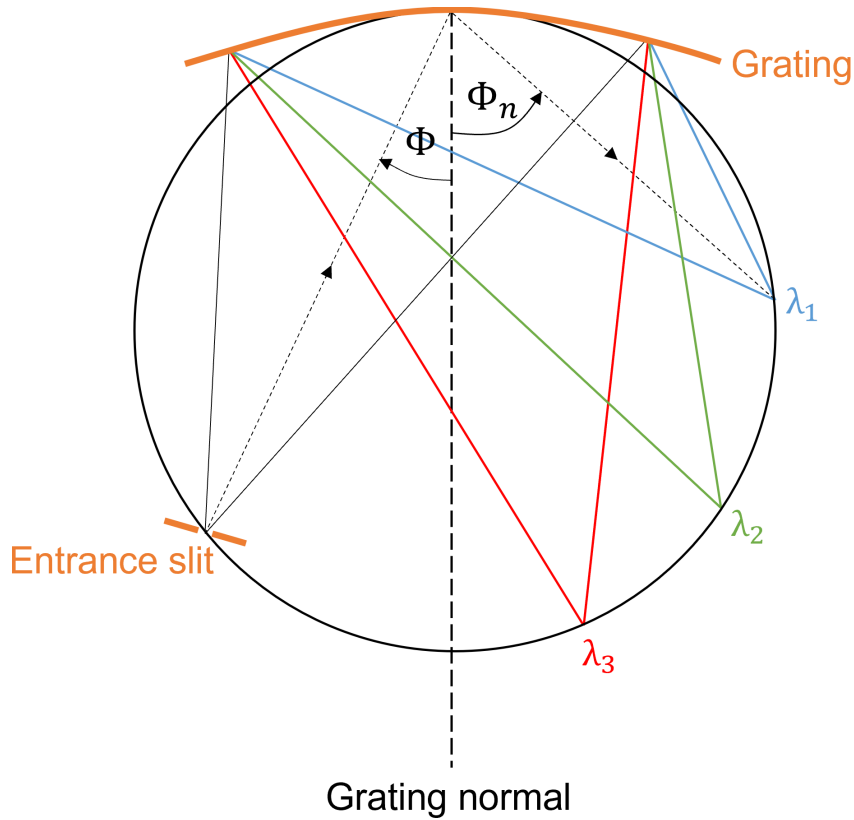


Figure 3.5.: Schematic diagram of Rowland geometry. Rulings and entrance slit E are perpendicular to the drawing plane. λ_1 , λ_2 and λ_3 indicate the focal positions of the spectrometer. The radius of curvature of the grating R is the same as the diameter.

where n represents the order of diffraction of interest as an integer, λ the wavelength, g the spacing of the grating, and ϕ equals the angle of incidence. Knowing the Rowland circle and the angle of incidence, the focal position can be determined geometrically by finding the intersection of the reflected beam with the Rowland circle.

Mechanical design

A circular diffraction grating made of platinum coated glass (2400 l/mm) with a diameter of 150 mm is used. The radius of curvature is $R = 3000$ mm with a slope error $\sigma_R < 0.4^\circ$, and the blaze wavelength is $\lambda_{opt} = 80$ nm [28].

With this grating, a normal-incidence Rowland configuration with an arm length of 3m between the trap and grating was chosen for the spectrometer. In this setup, no entrance slit or focusing optics were used. By using the ion cloud as a cylindrical light source,

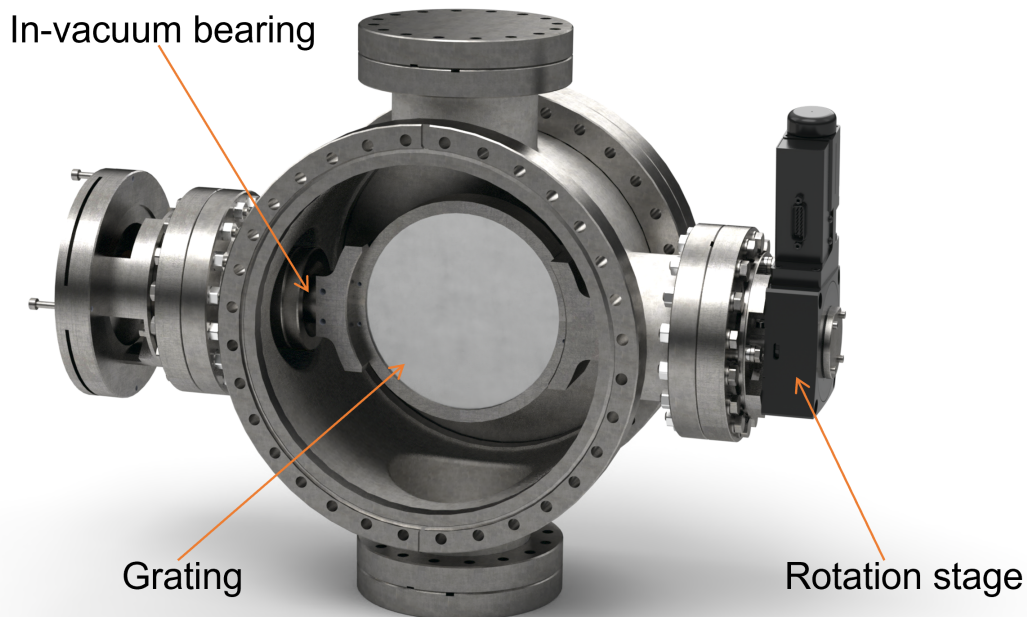


Figure 3.6.: Rendered image of the grating mount.

maximum light-efficiency is achieved. The angle between incident and reflected light is fixed to $\alpha = 15^\circ$ due to the dimensions of the FLASH EBIT. By rotating the grating with respect to the incident light, the observed spectral range is changed. Therefore, the detector needs to move closer or further away from the grating, to stay in the focal plane on the Rowland circle. To achieve this movement, the detector is placed on a linear manipulator stage below the trap's supporting structure.

To ensure precise rotation in the vacuum, a ferro-magnetic fluid rotary feed-through is used. A shaft connected to the grating holder is sealed by a ferrofluid, which is kept upright by a magnetic field. On the inside in vacuum, precise positioning is facilitated by unlubricated ball bearings.

Outside the vacuum, a Newport URS75BPP rotation stage is used for positioning. For precise measurement of the grating angle, a Heidenhain RON 905 rotary encoder is used.

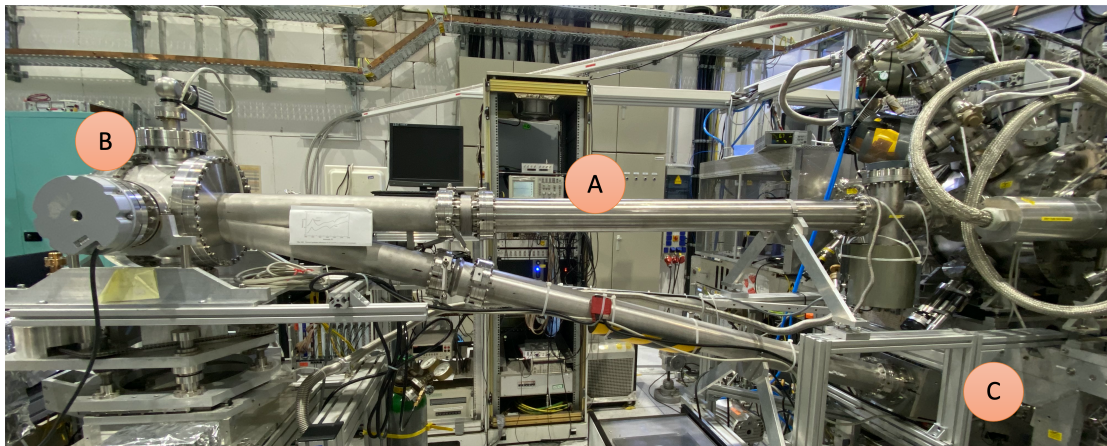


Figure 3.7.: A photograph of the VUV spectrometer. Radiation from the ions in the FLASH EBIT passes the 3m arm (A) and hits the grating in the grating mount (B) where it is refracted and focused to be observed with the ORFEUS detector.

ORFEUS detector

In general, there are several detector options when it comes to detection of VUV radiation. For the 3m-NIM-spectrometer a microchannel plate (MCP) detector is used. This kind of detector has several advantages. On the one hand, it is position-sensitive, which is preferred since it reduces acquisition time radically compared to a spectrometer with an exit slit and detector without spatial resolution. On the other hand, only a small spectral range is covered at a specific grating angle, therefore only a few lines are detected at once. To measure a wide-range spectrum, the grating is rotated continuously, making timing information crucial for data evaluation, which can be supplied by the MCP. Additionally, the MCP detector is blind for radiation in the visible regime, meaning background light from i.e. pressure gauges is not contributing to the counting rate. The kind of detector used here, consists of two main components: the microchannel plate and a wedge-and-stripe anode (WSA). MCPs are plates with microscopically small bundled electron multiplier channels, which are made of glass [6]. The top and bottom of the MCPs are equipped with metallic electrodes and a voltage of typically 1000 V is applied there to induce an homogeneous electric field. The inner channel surfaces are coated with semiconducting material. If a UV-photon strikes the channel surface, it can trigger a photo-electron (in vacuum). The electric field accelerates the electron towards the back of the MCP, and the electron will hit the channel wall again, triggering several electrons. At the back of the MCP, an electron cloud emerges. From each channel 10^4 electrons can emerge (see Fig. 3.9).

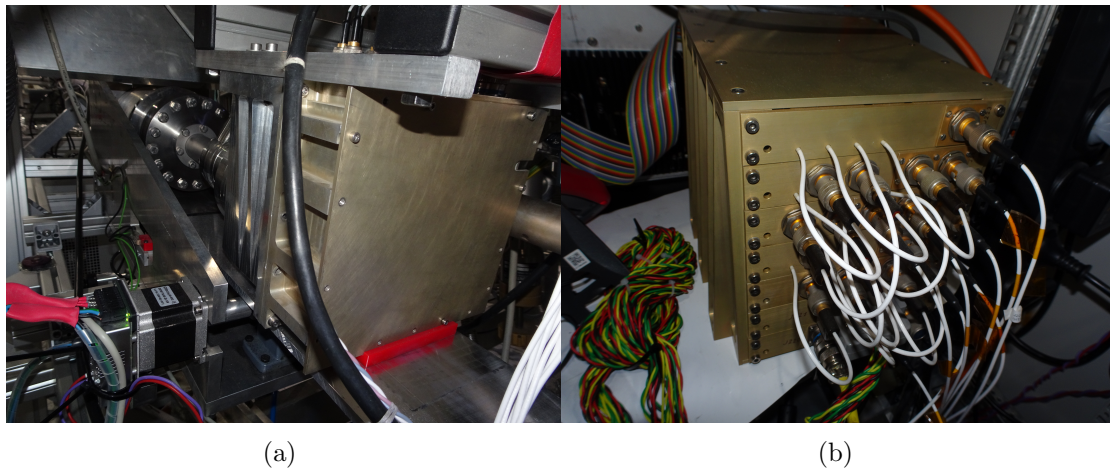


Figure 3.8.: (a) is a photograph of the ORFEUS detector that is located below the magnet chamber of the FLASH EBIT. (b) is a photograph the corresponding charge amplifier that is connected to the the anode.

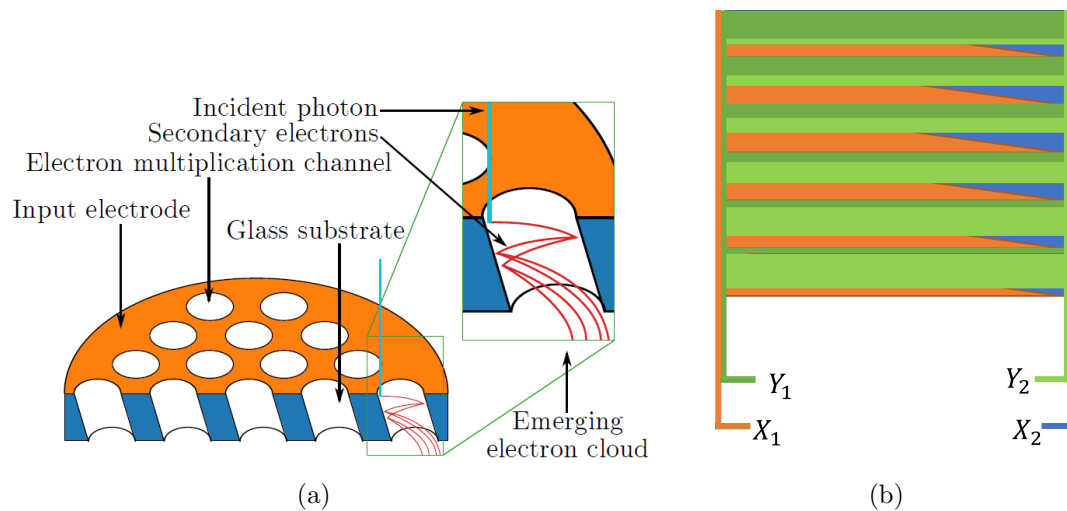


Figure 3.9.: (a) is a schematic diagram of a micro channel plate. When a photon of sufficient energy impinges on a micro-channel wall, it can cause an emission of an electron. This electron induces the emission of secondary electrons. After several multiplication steps, an electron cloud emerges that hits the wedge-and-stripe (WAS) anode (b), which determines the hit position.

After exiting the MCP, the electron cloud hits the wedge-and-strip anode, which consists of a gold-coated quartz plate. A pattern of four interlocking conductor tracks in the form of wedges and stripes was etched into it, giving this type of anode its name. The incident electron cloud is distributed over all 4 conductor tracks, which leads to a charge distribution that is specific for the point of impact. Therefore, the impact coordinates of the registered photon are provided, which are processed by a digital position analyzer (DPA).

The installed detector was build for the space telescope ORFEUS (german: Orbitales und rückführbares Fern- und Extrem-Ultraviolett-Spektrometer), which is the root to its name ORFEUS detector. The MCPs for the ORFEUS detector are custom-made by Hamamatsu Photonics. Three MCPs connected in a series are used, resulting in a high amplification of 10^7 to 10^8 electrons per photon. The diameter of the MCPs is 60 mm, and the diameter of a channel is $12\ \mu\text{m}$. The field of view of the detector is limited to an area of $40\ \text{mm}^2 \times 40\ \text{mm}^2$. The anode has a $2\ \mu\text{m}$ -thick gold layer and has an active area of $44\ \text{mm}^2 \times 44\ \text{mm}^2$.

Data acquisition system

In the data acquisition (DAQ), two computers are involved: a spectrometer control and a dedicated data acquisition computer that is connected to the detector. Both of them record data that is crucial for analysis.

The data acquisition computer has to switch on the high voltage (HV) for the detector, in order to record data. The ORFEUS-detector outputs the detected events in the form of four voltage pulse signals: X_1 , X_2 , Y_1 and Y_2 . Those voltage pulses are processed by the digital position analyzer by first digitizing them, and next calculating the positions of the detected events. The location is transferred to the data acquisition computer, where the events are recorded.

The spectrometer control computer is communicating with a Newport SMC100BPP motion controller to steer the Newport URS75BPP rotation stage. While the incident angle of the grating is changing, the Trinamic PD-109-57 focus motor is moving the linear stage continuously, to keep the detector in the focal plane. Since the guaranteed accuracy of the rotation stage is limited to 0.015° , it is mechanically connected to a Heidenhain RON 905 rotary encoder with one absolute position and 36 000 incremental impulses per rotation.

The encoder data is read out by a Heidenhain AWE 1024 encoder controller, which

Table 3.1.: Properties of the Hitachi flat-field grating used in the EUV spectrometer [29]

R	Θ	r	r'	α	β_1	β_2	$\lambda_2 - \lambda_1$	L
[mm]	[°]	[mm]	[mm]	[°]	[°]	[°]	[nm]	[mm]
13450	1.9	564	563.2	87	75.61	83.04	5-25	75.73

interpolates 1024-fold, resulting in a final angular resolution of better than $0.000\,001^\circ = 10^{-6}^\circ$. It is connected to the data acquisition computer, which ensures that the rotation angle and the recorded events receive their time stamps synchronously.

3.2.2. EUV spectrometer

The second spectrometer the EBIT is equipped with, is the extreme-ultraviolet spectrometer. Unlike the VUV normal-incidence spectrometer described above, the EUV spectrometer has an aberration-corrected, concave, grazing incidence flat-field grating, produced by the company Hitachi [29].

Hitachi flat-field grating

The Hitachi flat-field grating consists of a glass substrate into which grooves are carved in. The surface is coated with gold to achieve an optimum reflectance. Moreover, the surface has a concave curvature radius R , hence the grating has not only dispersive properties, but is also able to focus the outgoing EUV rays. The grooves are made under a blaze angle θ in varying distances $d(x)$ over the length x of the grating. Furthermore, the grooves are curved over the width y of the grating. This results in the light being focused on a flat-field instead of a circle, which is in contrast to the VUV spectrometer with the Rowland circle concept. This way, aberrations like coma and spherical aberration are corrected. Fig. 3.10 shows schematically the most important quantities.

The radiation comes from the ions in the EBIT at the distance r from the grating. The EUV rays hit the grating at an angle α with respect to the grating normal. They are reflected with the angle β , that depends on the wavelength λ of the rays, onto the focal plane at a distance r' . From geometric considerations using (3.1), the wavelength-dependant image positions can be calculated, where the image position for λ_1 has the distance L to the position of the wavelength λ_2 . The corresponding quantities for the Hitachi grating can be found in Table 3.1, more specifics are discussed in [30]. By using

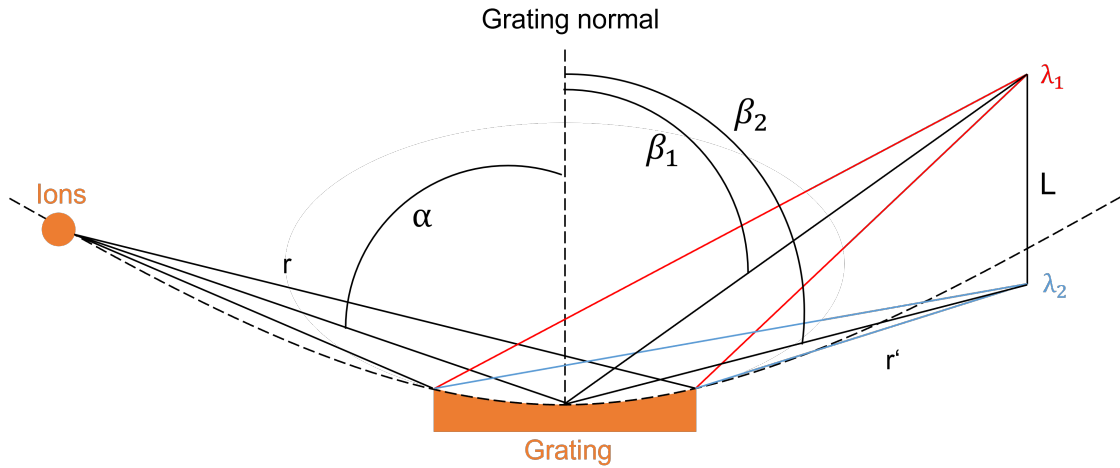


Figure 3.10.: Diffraction of the emitted light for two different wavelengths. The angle of incidence is α and the diffraction angles β_1 and β_2 are the extreme angles for which the resulting image is focused correctly.

(3.1) the linear dispersion $dz/d\lambda$ on the focal plane can be derived

$$\frac{dz}{d\lambda} = r' \frac{d(\beta_2 - \beta_1)}{d\lambda} = 3.8 \frac{mm}{nm}. \quad (3.2)$$

Besides the geometry of the grating, the spectral resolution of a spectrometer also depends on the size of the entrance slit. The EUV spectrometer is operated without an entrance slit at the EBIT, it only uses the narrow spatial expansion of the ion cloud/electron beam as an alternative. The advantage of this method is the simple setup and the prevention of intensity losses by looking directly into the trap. Additionally, the 0th-order of the ion cloud can be displayed and the spatial expansion of the electron beam can be determined by measuring the width of the spectral lines. A disadvantage is that the achievable resolution is restricted since the spatial expansion of the electron beam is fixed.

Delay-line detector

The currently installed detector is the RoentDek DLD40 delay-line detector, which can detect multiple photon hits and analyze the position and time coordinates for each individual hit. Like the ORFEUS-detector, it uses a microchannel plate (MCP) which provides the electron showers that are detected, but instead of a wedge-and-stripe anode, a delay-line anode is used for detection. It consists of two wires with parallel narrow

windings, which are arranged perpendicular to each other. A schematic depiction can be seen in Fig. 3.12. If an electron shower hits the wire, a pulse is sent in both wire directions. By measuring the time difference between the two pulses when they reach the wire ends, the position of the impact on the wire can be determined. By analyzing both wires, an accurate position in two dimensions can be found. A more detailed explanation towards the time recording, the characteristics of the DLD40-MCP detector and the data acquisition, can be found in [31].

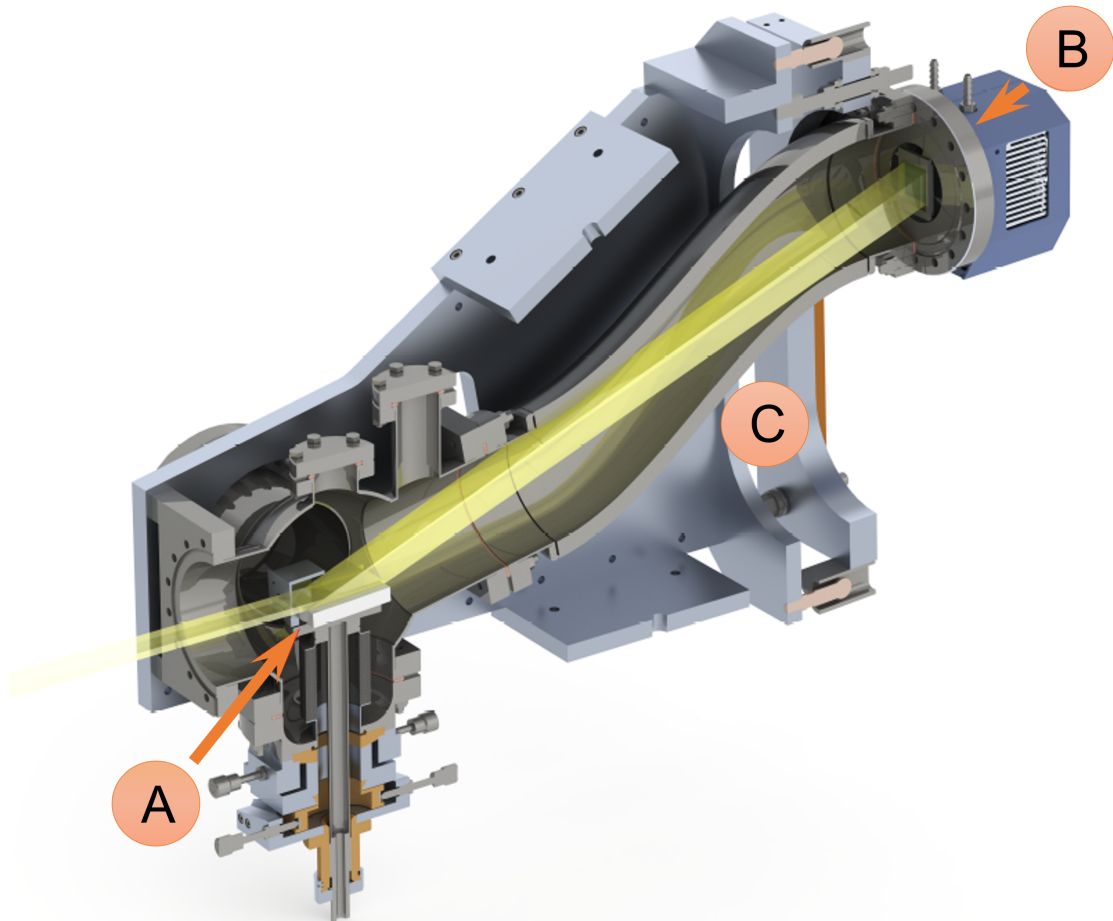


Figure 3.11.: Section of the flat-field EUV spectrometer. Radiation emitted by the ions in the trap propagate from left to right, which is indicated by the yellow beam. (A) denoted the grating located on a tilt-shift stage for alignment. (B) is a CCD camera that was exchanged for the RoentDek DLD40 delay-line detector. (C) is a edge-welded bellow that is needed since the detector position can be changed, in order to cover a different range of wavelengths. Taken from [26].

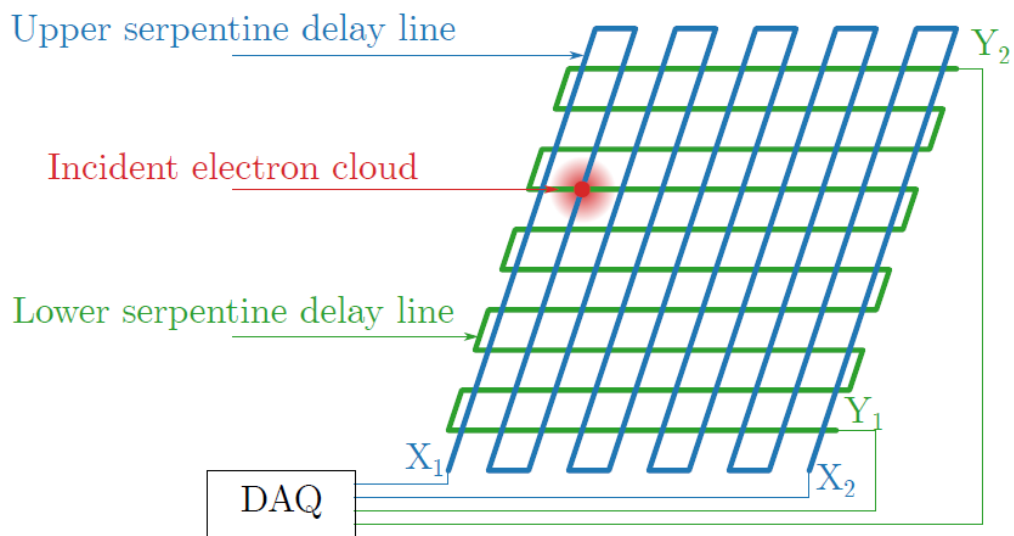


Figure 3.12.: Schematic diagram of a delay-line anode. When an electron cloud hits the anode, current pulses are propagating in both wire directions. The data acquisition system (DAQ) analyzes the time delay between the incoming pulses, determining the incident position of the electron cloud. Taken from [26].

4. Focus optimisation of the ORFEUS detector

As described in 3.2.1, the grating is rotated to measure wide-range spectra. In order to obtain focused lines, the ORFEUS detector is positioned on a linear stage to move the detector into the respective focus position while the grating is rotated. Since the detector was installed and put into operation for the first time for this work, a program, that moves the detector automatically to the right position for a given grating angle, was still missing. To provide a program like this, the focus positions for several angles have to be determined manually first. By interpolating the determined motor positions, a fit function is received that can be implemented into a respective software.

4.1. Measurement scheme

To move the linear stage manually, the data acquisition computer is connected to the motor of the linear stage ¹, and to the RON ² that acquires the incident angle of the grating. The spectrometer computer is connected to the rotation stage of the grating³ and a software that allows to set the grating angle is used ⁴. Further, a program that allows to move the detector on the linear stage to a specific motor position is used ⁵.

Implementation of the interpolation into a program requires manual determination of the optimal motor positions for several spectral lines. This is achieved by slowly rotating the grating, while observing the photon count rate (intensity), which significantly increases when grating equation is fulfilled, connecting the potential line with the corresponding angle. Subsequently, a single line is inspected by keeping the grating angle fixed. To depict and inspect the lines, a software ⁶ is used that retrieves signal

¹by using `start_server_focus.py`

²by using `start_server_ron.py`

³`start_server_rotstage.py`

⁴graphical user interface (GUI) `main.pyw`

⁵graphical user interface (GUI) `MotorSoftver3.0.ui`

⁶`Erfassung_VSmx.exe`

positions from the DPA that were acquired by the ORFEUS-detector, as explained in 3.2.1. For a measurement for a fixed angle, the option ‘Vollintegration’ in the software is used. Here, a black square that represents the surface of the detector appears, and the acquired signals pop up in real time at the specific positions they were measured at. After a sufficiently long integration time, the individual signals form a line. When the measurement is stopped, the depicted signal positions are saved in a binary interleaved file (.bil), and can be investigated in a program that analyzes the line widths. The program used for this work ⁷ sums up the line signal vertically, and has the feature to fit a gaussian function to the resulting peak, providing the line width. Fig. 4.1 shows an example of a line while unfocused (a) and focused (b).

4.2. Interpolation of the motor focus positions

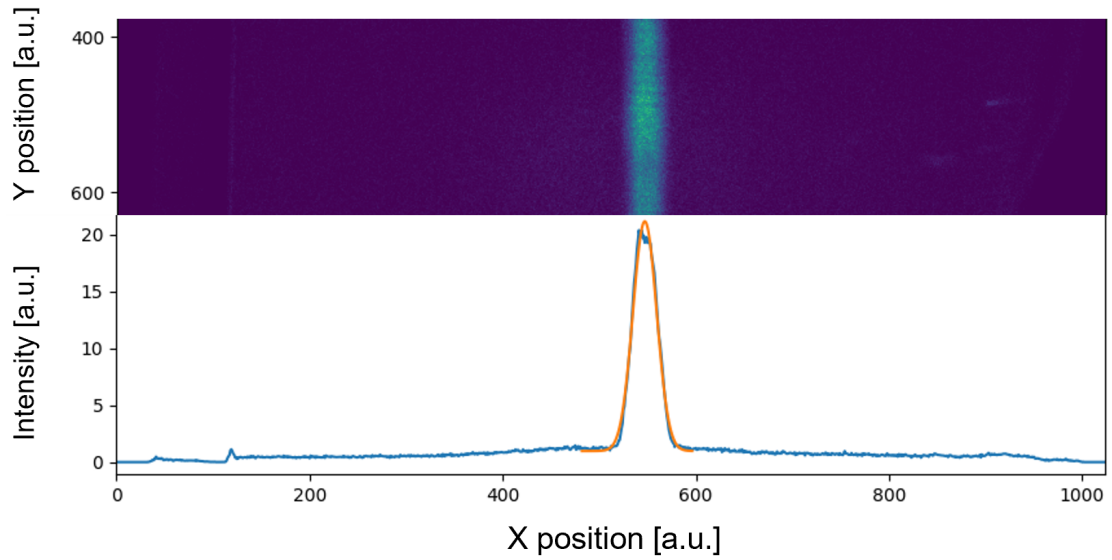
For the data interpolation, measurements of lines at several angles at different motor positions were taken, while the integration time was kept constant ($t = 4$ min). Using the previously described program, the different line widths were measured for each of them. The motor position was fine tuned to optimize the focus as accurately as possible for a given incidence angle. After analyzing several lines with this procedure, the determined focus positions for given incidence angles were fitted to a parabola function to obtain the interpolation-equation:

$$y(\alpha) = (-0.031 \pm 0.004) \cdot \alpha^2 - (0.493 \pm 0.072) \cdot \alpha + (3.911 \pm 0.233), \quad (4.1)$$

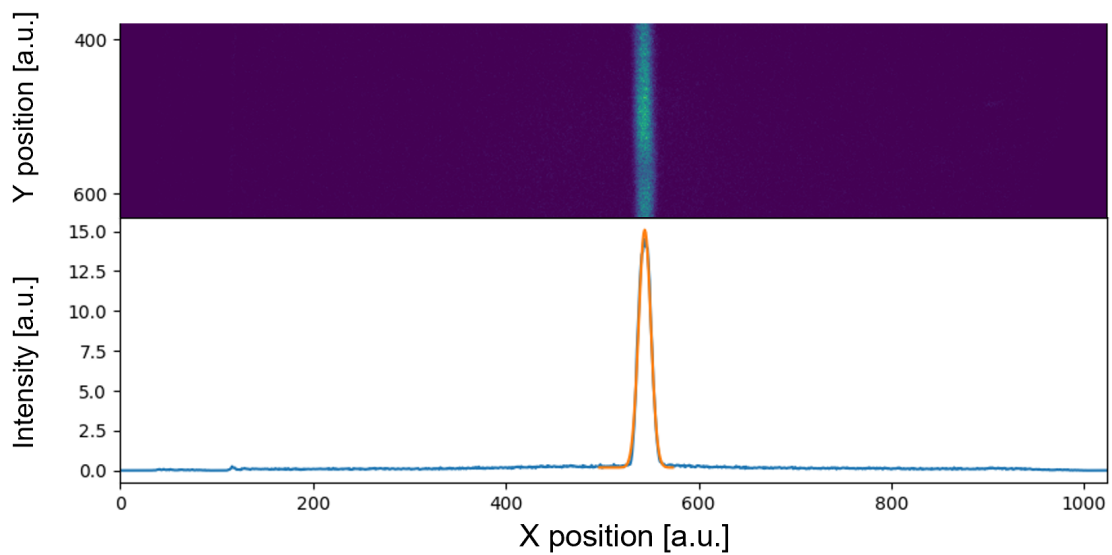
where α is the incidence angle and $y(\alpha)$ is the motor position in millions of steps. The resulting interpolation was then implemented in program ⁸ that is moving the motor into the right position to obtain focused lines automatically, even while the grating is in motion.

⁷BIL_analysis_tool.py

⁸autofocus_28042021.py



(a)



(b)

Figure 4.1.: An example of the output of the used software. The upper part of (a) shows a picture of the line measured by the detector, while the lower part shows the over the pixel summed intensities in arbitrary units. This division also applies to (b). While (b) shows the line while the detector is in focus, (a) shows a wider line due to the wrong detector position.

5. Iron Spectroscopy

As discussed in Chapter 1, iron spectra observed at white dwarfs – especially of the charge state Fe V – acquired a special significance in terms of justifying Physics beyond the Standard Model, as they were used to calculate a variation of the fine structure constant α [11]. Therefore, this work was dedicated to iron spectroscopy, trying to record Fe V spectra. Therefore, this chapter deals with the recording, calibration and analysis of wide-range spectra acquired by the VUV spectrometer.

5.1. DR measurement

Before wide-range spectra were acquired with the VUV spectrometer, the EBIT was tuned to obtain bias beam energy of 2040eV , and a program was used to continuously increase the electron beam energy up to 7040eV , in order to observe DR resonance processes. Knowing the specific DR resonance energies for iron, the existence of iron inside the trap was checked and proven, since several different DR processes for iron were measured (see Fig. 5.1). Afterwards, the energy ramp was turned off, resulting again in a beam energy of 2040eV . At this energy, helium-like and lithium-like iron ions were produced, as the most prominent lines from these transitions were measured with the EUV spectrometer (see Fig. 5.2). to make sure iron was inside the trap. 2nd order searched verweis appendix energien

5.2. Measurement scheme

For the wide-range spectra measurements, the same software as explained in 4.1 is used. The software ¹ that allows to set a fixed angle, also has the option to run an uploaded python script, where an angle range can be set which is going to be scanned back and forth, continuously ². While the script is running, the scanned angles are saved with

¹graphical user interface (GUI) main.pyw

²aufundab.py

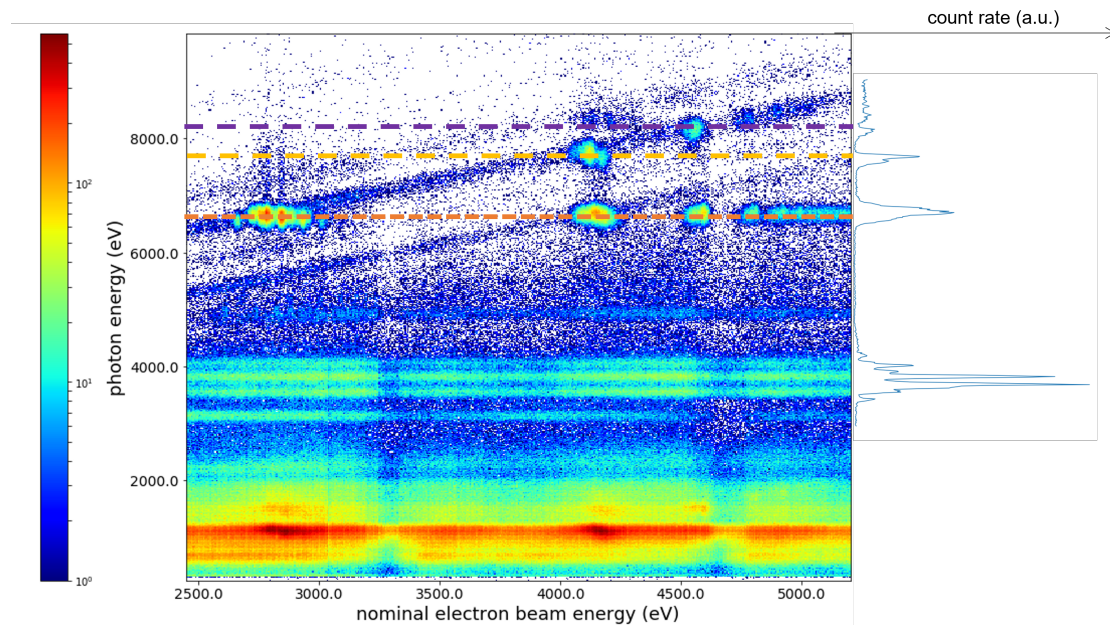


Figure 5.1.: This graph shows the 2D plot of the photon energy as a function of the nominal electron beam energy that was ramped. The different intensities are indicated by different colors. Further, it shows a 1D projection for the vertically summed signal. The DR resonances are depicted as dashed lines, where the orange line represents the DR processes from K shell to L shell, the yellow line represents the DR processes from M to K and the violet line represents the DR processes from N to M shell. From left to right, the light spots in the 2D plot represent the KLL-, KLM-, KLN- and KLO-DR processes.

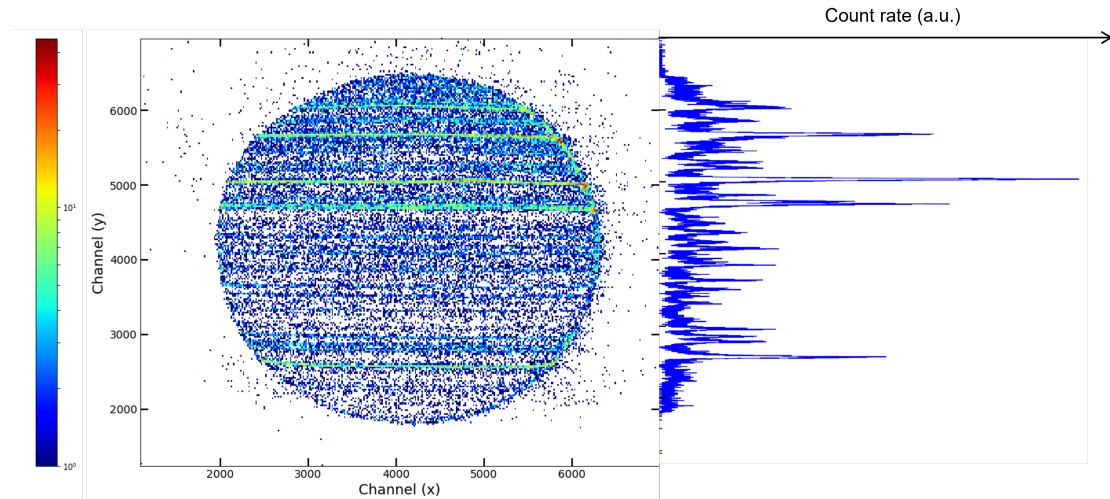


Figure 5.2.: This graph shows a 2D plot of a spectrum measurement taken with the EUV spectrometer and the different intensities are indicated by different colors. The x- and y-axes are given in terms of channels, since a calibration was waived due to time constraints. On the right side, a 1D projection of the vertically summed spectrum is shown. The prominent peaks were identified as different Fe XX IV and Fe XX III transitions by experience.

a respective time stamp into an encrypted database file (‘.db-file’). Simultaneously, on the data acquisition computer the software that acquires the photon signals from the detector is run ³. The measurement mode for wide-range spectra acquisition in the used program is called ‘Integration in File’, which saves the photon signals with their respective time stamps in a photon listing file(‘.phl’) and a high dynamic range file (‘.hdr’) format together with the exposure time per angle. To assess the acquired data, the described files are decrypted and the timestamps of the measured angles are matched to those of the detected photon signals with a specific program ⁴. By dividing the signal strengths by the respective exposure times, a normalised count rate for the whole spectrum is achieved. The matched angles and count rates are then saved as comma-separated values (‘.csv’-file), in order to depict the data later.

5.3. Experimental parameters

Before each wide-range spectra measurement, the spectrometer was moved to the 0th-order to optimize the parameters at the EBIT. First, the approximate beam energy was

³Erfassung_VSmx.exe

⁴createspectrum.py

Setup I	
Cathode bias [V]	1910
Trap[V]	0-50-50-210-130-100-60-0-300
Beam energy [eV]	2040
Beam current [mA]	180
Dump	1s every 15s
Setup II	
Cathode bias [V]	900
Trap[V]	0-30-30-100-60-100-40-0-300
Beam energy [eV]	960
Beam current [mA]	125
Dump	1s every 13s
Setup III	
Cathode bias [V]	120
Trap[V]	0-0-0-0-30-0-0-0-300
Beam energy [eV]	150
Beam current [mA]	3.5
Dump	1s every 15s

Table 5.1.: EBIT parameter settings for the in this work presented spectra

set with respect to the intended charge state of iron ions, before carefully varying the drift tube settings to maximise signal intensity and oxygen suppression (see Table 5.1). After optimising the parameters, wide-range iron spectra were taken at different energy levels to obtain lines of a specific charge state of interest. As described in Chapter 1, spectral lines of Fe V are of special interest, therefore, several measurements at different energies were taken to find them. Also, more measurements were taken to find the 2nd-order of He-like and Li-like iron. The general exposure time per measurement varied between one and three days to ensure a sufficiently high signal-to-noise ratio at every angle.

5.4. Calibration

To assess the spectra acquired by the VUV spectrometer, the incident angle has to be converted into wavelengths first. This is done by identifying well-known prominent lines and assigning them a respective incident grating angle. To ensure a precise calibration, it is useful to take 2nd-order lines and symmetric lines on the other side of the 0th-order into account.

Table 5.2.: A list of the oxygen lines used for calibration from NIST and the corresponding incidence angle positions and errors

Calibration line λ_{NIST} [nm]	$\Delta\lambda_{\text{NIST}}$ [nm]	Angle [°]	Angle error [°]
O VI 1 x 103.1912	(25)	-1.09096	(16)
O VI 1 x 103.7613	(25)	-1.05126	(36)
O IV 1 x 60.9829	(25)	-4.03112	(26)
O V 1 x 62.9732	(25)	-3.89173	(2)
O IV 1 x 78.7710	(25)	-2.79303	(10)
O IV 1 x 79.0109	(25)	-2.77596	(8)
O VI -1 x 103.7613	(25)	-15.47665	(2)
O VI -1 x 103.1912	(25)	-15.43676	(3)
O V -1 x 62.9732	(25)	-12.63147	(2)
O IV -1 x 60.9829	(25)	-12.49250	(54)
O IV -1 x 79.0109	(25)	-13.74906	(43)
O IV -1 x 78.7710	(25)	-13.73165	(10)
O V 2 x 62.9732	(25)	0.50024	(3)

For the calibration of the following spectra, a measurement with the EBIT parameter setup I from Table 5.1 and a total exposure time of one day for a range of 22° around the 0^{th} -order was analyzed. Since oxygen lines are often very prominent and frequently found in measurements from other detectors connected to the FLASH EBIT, and since oxygen is also injected along with the liquid compound, both iron (Fe) and oxygen (O) lines could be identified. The wavelength data was provided by the National Institute of Standards and Technology (NIST) Standard Reference Database version 5.8 [32]. A gaussian function was fitted to the oxygen peaks to obtain the peak positions angles to the corresponding wavelengths. The identified lines are displayed in Table 5.2, and the measured spectrum together with the calibration lines is depicted in Fig. 5.3.

In Fig. 5.4 the wavelength as a function of the grating angle is plotted, and the calibration points are displayed as black squares. To find an interpolation function that describes the dispersive relation from the spectrometer properly, polynomial functions of the orders 1 – 4 were fitted and compared to each other. By assessing the residual plots for the different fit functions in Fig. 5.4 one can see that not all data points are located in the confidence intervals for the linear and parabolic fit. This suggests that a polynomial fit of higher order is required to describe the data with sufficient high accuracy. The confidence bands for the cubic and 4^{th} -order polynomial both seem to contain all the data points, but the confidence band for the 4^{th} -order polynomial is much wider than the confidence band of the cubic function, which indicates that a polynomial function

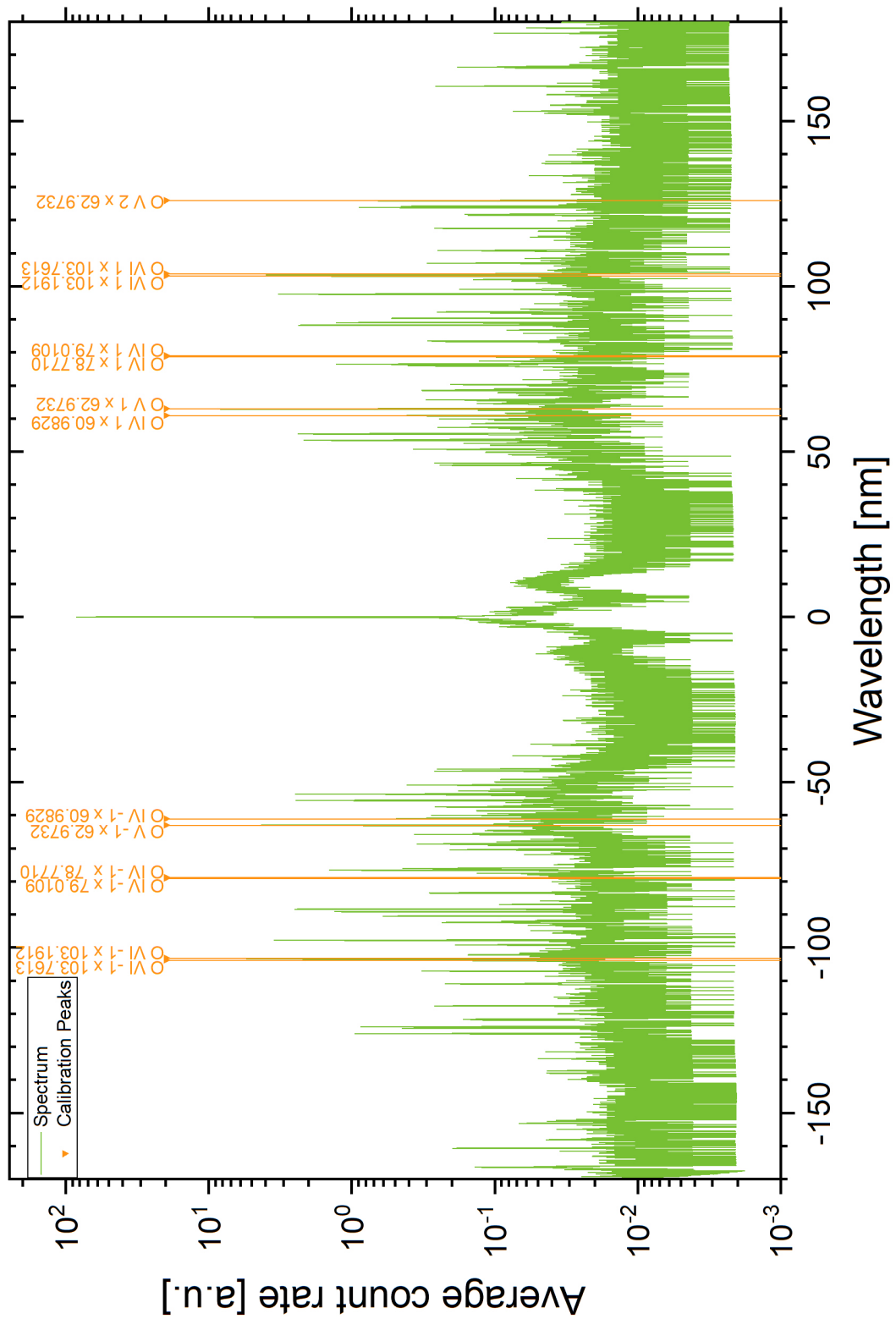


Figure 5.3.: The acquired spectrum for an electron beam energy at 2040 eV with the identified calibration lines.

of 4th-order is overfitting the dispersive relation. Additionally, the residual of the cubic function was investigated further and all data points were in the confidence interval (see Fig. 5.5). Therefore, the cubic polynomial was chosen to provide the conversion from the measured angle to the corresponding wavelength.

To get an accurate estimate of the calibration uncertainty, the final calibration function $f(x)$ was determined in two steps. First, an unweighted fit was used to get an approximation of the calibration function, the obtained fit parameters can be found in Fig. 5.4. By differentiating this result with respect to the angle, a dispersion for any grating angle is received. Multiplying this value with the uncertainties for the line positions Δx obtained from the Gaussian functions for the individual peaks in the spectrum, uncertainties in y for the wavelengths are calculated for each data point. Since the uncertainty of the line fit is independent of the wavelength uncertainties λ_{NIST} in the NIST atomic spectra database, they can be added using the root sum squared:

$$\Delta y_i = \sqrt{\left(\left.\frac{df(x)}{dx}\right|_{x=\mu_i} \Delta \mu_i\right)^2 + (\Delta \lambda_{NIST})^2} \quad (5.1)$$

These combined values are used as weights in a second fit of the cubic polynomial, resulting in the final calibration function:

$$f(x) = (-7.5 \pm 0.1) \cdot 10^{-4} \frac{\text{nm}}{\text{o}^3} \cdot x^3 - (1.8 \pm 0.1) \cdot 10^{-3} \frac{\text{nm}}{\text{o}^2} \cdot x^2 \\ + (14.4238 \pm 0.0007) \frac{\text{nm}}{\text{o}} \cdot x + (18.179 \pm 0.003) \text{ nm} \quad (5.2)$$

5.5. Spectra analysis

After calibration, the spectrum taken with the FLASH EBIT parameters from setup I (ref auf Tabelle) was investigated further since it contained the several peaks that were suspected to be Fe V lines. By fitting a Gaussian function to the detected peaks and comparing the measured wavelength to data provided by NIST [32], around 500 lines from several elements and charge states could be matched (see Table A.1). For this, several elements and charge states were taken into account that were assumed to be inside the FLASH EBIT. Besides iron (Fe), the injected liquid compound iron pentacarbonyl ($\text{Fe}(\text{CO})_5$) also contains oxygen (O) and carbon (C). The thermionic dispenser cathode is made of tungsten (W) and barium (Ba), therefore, these elements could have found their way into the EBIT, even though a dump was used to dislodge them. Furthermore,

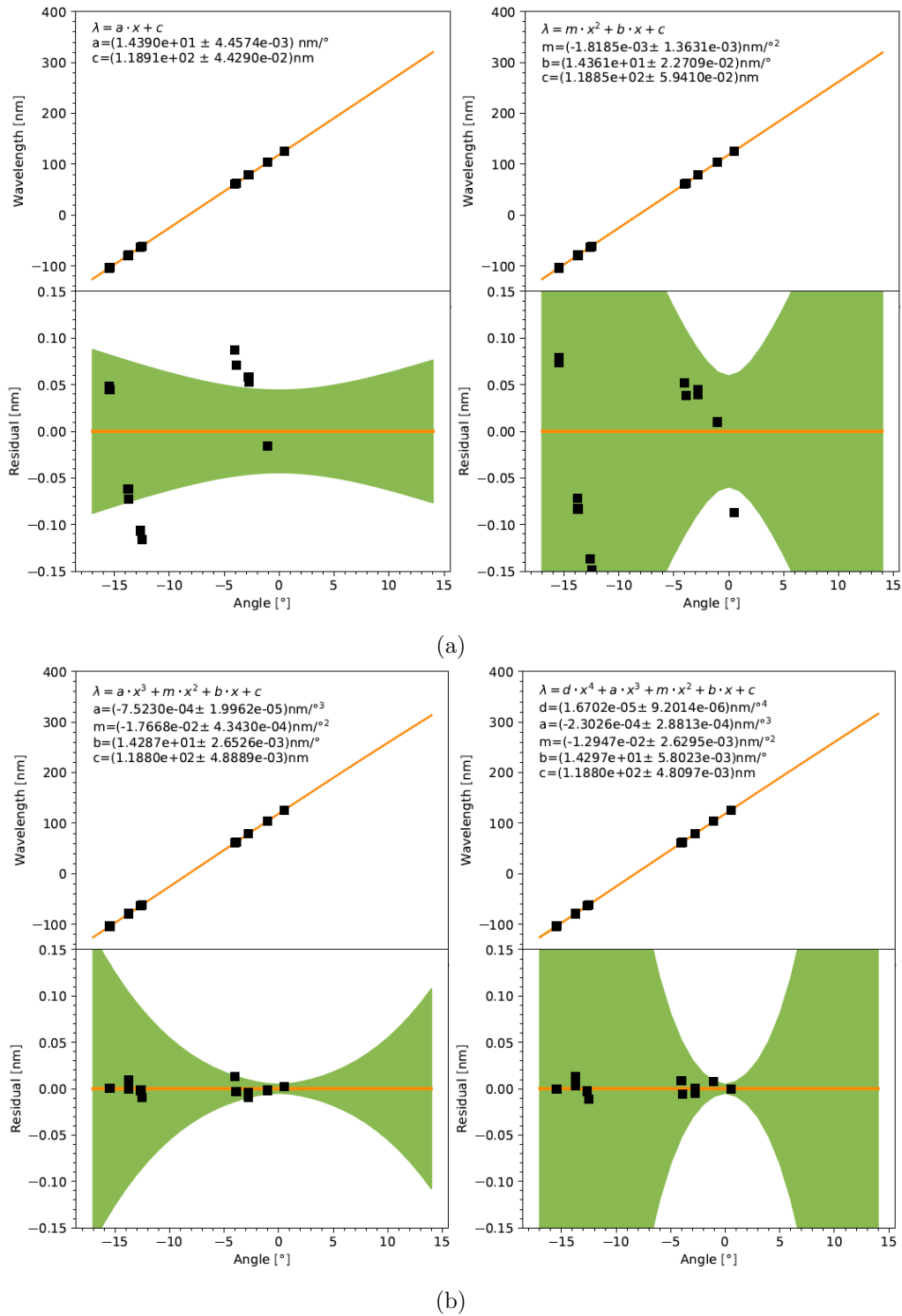


Figure 5.4.: The upper parts of this 4 graphs show the calibration data as black squares, the interpolation function is orange, and the confidence band is green. Below each graph, the respective residual plot is located. (a) shows the graphs for the polynomial interpolation functions of the orders 1 and 2, and (b) shows the remaining orders 3 and

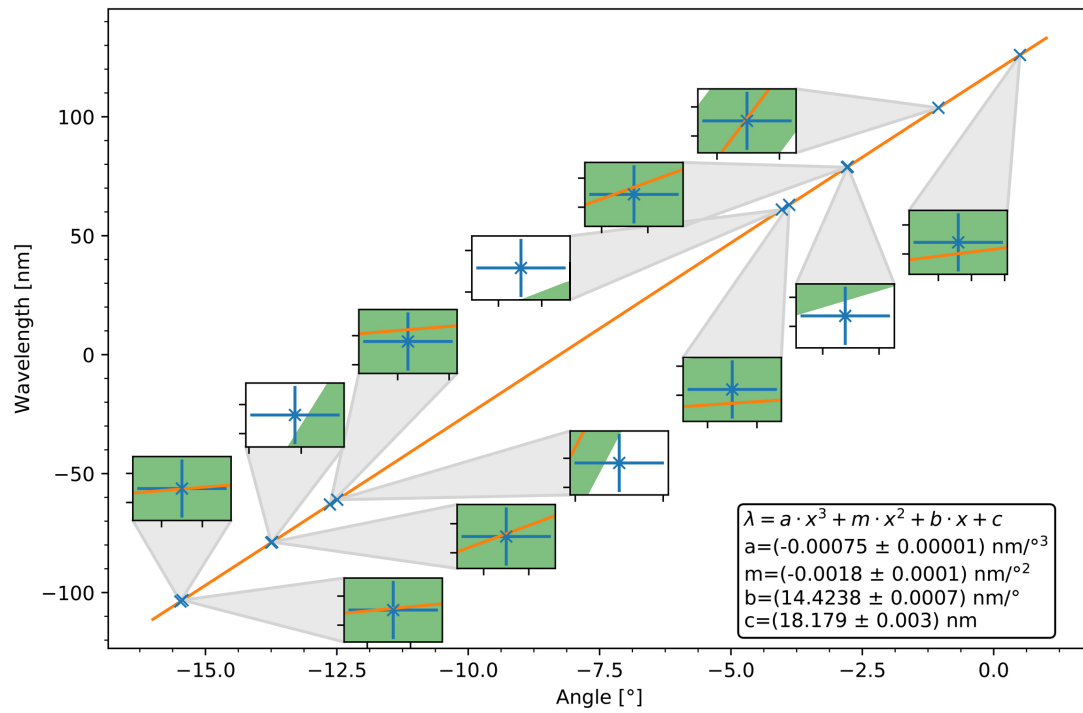


Figure 5.5.: A plot of the interpolation for the polynomial function of order 3, which shows each calibration point with the respective error bars zoomed in. The calibration points and error bars are depicted in blue, the fit function is orange, and the confidence band is green. The plot

the vacuum inside the FLASH EBIT is not perfect ($P \approx 5 \cdot 10^{-10}$ mbar), air remnants in form of nitrogen (N) have to be considered. Additionally, elements from previous measurements have to be taken into account, so the data was also checked for argon (Ar) lines.

Because of the injected compound, several prominent lines of different charge states of oxygen and carbon could be detected. Due to evaporative cooling lower charge states were favored, therefore O III – O V and C III – C IV lines dominated for these elements (see Table A.1). Lines of even lower charge states for these elements were suspected as well for certain peaks, but weren't included in the table due to careful consideration of the relative intensities and transition strengths provided by NIST, since supposedly more prominent lines of the same charge state could not be detected in the spectrum.

For iron, the energy beam was set sufficiently high to produce helium-like and lithium-like charge states of iron as explained in Section 5.1. The strongest $K\alpha$ transitions for these ions were expected to be seen in 2nd-order in the spectrum. These lines could unfortunately not be detected, so it seems that the signal strength in 2nd-order of the expected lines was not sufficiently high. Nevertheless, multiple lines originating from iron ions were found for the charge states Fe III and Fe V, as well as some few for Fe II. A reason for the favoured lower charge states could be a too high injection pressure while the measurement was taken. Although the identification of the lines was again done under consideration of the relative intensities and transition strengths provided by NIST, the identified iron lines for the relevant charge states have to be assessed critically and questioned. Fe III and Fe V have thousands of possible transition, therefore, in a range of a few nm hundreds of lines with similar intensities exist. The provided relative intensities suggest prominent transition lines that could not be detected, while lines with a lower relative intensity were identified – with no alternate element or charge state that have a transition matching the measured peak. Therefore, the accuracy of the relative intensities has to be questioned as well. First of all, the relative intensities from NIST had to be estimated by considering measurements taken by different spectrometers sensitive for different spectral ranges. Further, the cross-section for a transition scales with the energy, therefore, certain transitions could have been favoured even though the relative intensity was estimated as low. A list of the suspected lines can be found in Table A.1. Further, a Gaussian function was fitted to the most prominent peaks in order to obtain their maximum positions. The wavelength uncertainties are given as the root sum square of the uncertainty arising from the determination of the maximum position for the respective line and the mean of the calibration fit residua. Several peaks contained more than one assigned line from NIST, therefore, only a total line width

for all of them could be determined. Said determined wavelengths and uncertainties with the respectively assigned wavelength data from NIST are presented in Table 5.3. To compare the analysed spectrum to spectra acquired at different beam energies, the Fig. 5.6 and 5.7 are provided. Both show three different electron beam energies due to different EBIT parameters, which can be found in Table 5.1 (setup I – III). Additionally, the oxygen lines that were calibrated are depicted, showing that at lower beam energies oxygen suppression is achieved. A detailed analysis of the other two spectra would go beyond the scope of this work, therefore it is not included.

Table 5.3.: A list of all fitted peak positions x and the respective NIST lines contained in the peaks, in the spectrum at 2040eV

Peak position x [nm]	Δx [nm]	Charge state	λ_{NIST} [nm]	$\Delta\lambda_{\text{NIST}}$ [nm]
31.245	(12)	C IV	31.2420	(10)
31.245	(12)	C IV	31.2460	(10)
38.433	(12)	C IV	38.4030	(10)
38.433	(12)	C IV	38.4180	(10)
45.957	(9)	C III	45.9460	(10)
45.957	(9)	C III	45.9520	(10)
45.957	(9)	C III	45.9630	(10)
46.581	(9)	O II	46.4785	(10)
46.581	(9)	O II	46.5760	(10)
50.796	(9)	O III	50.7391	(10)
50.796	(9)	O III	50.7683	(10)
50.796	(9)	O III	50.8182	(10)
52.587	(9)	O III	52.5795	(10)
52.981	(11)	O VI	52.9883	(10)
52.981	(11)	O VI	52.9919	(10)
53.520	(9)	C III	53.5288	(10)
53.835	(9)	C III	53.8080	(10)
53.835	(9)	C III	53.8149	(10)
53.835	(9)	C III	53.8312	(10)
55.440	(9)	O IV	55.3330	(10)
55.440	(9)	O IV	55.4075	(10)
55.440	(9)	O IV	55.4514	(10)
55.440	(9)	O IV	55.5261	(10)
57.422	(9)	C III	57.4281	(10)
58.570	(9)	C III	58.5662	(10)
58.570	(9)	C III	58.5499	(10)
58.570	(9)	C III	58.5610	(10)
59.960	(9)	O III	59.9598	(10)
61.674	(11)	O IV	61.6952	(10)
61.674	(11)	O IV	61.7005	(10)
61.674	(11)	O IV	61.7036	(10)
62.573	(11)	O IV	62.4617	(10)

62.573	(11)	O IV	62.5130	(10)
62.573	(11)	O IV	62.5852	(10)
67.915	(10)	Fe III	67.9124	(100)
68.614	(10)	Fe III	68.5454	(100)
69.054	(10)	C III	69.0521	(100)
70.030	(11)	Fe III	70.0130	(100)
70.030	(11)	Fe III	70.0571	(100)
70.030	(11)	Fe III	70.1024	(2)
70.331	(10)	O III	70.2332	(2)
70.331	(10)	O III	70.2822	(5)
70.331	(10)	O III	70.2899	(2)
70.331	(10)	O III	70.3850	(2)
70.755	(13)	Fe III	70.7434	(2)
70.755	(13)	Fe III	70.7808	(2)
71.847	(11)	Fe V	71.7906	(2)
71.847	(11)	Fe V	71.7954	(2)
71.847	(11)	Fe V	71.8659	(2)
76.034	(10)	O V	75.8678	(2)
76.034	(10)	O V	75.9441	(2)
76.034	(10)	O V	76.0228	(2)
76.034	(10)	O V	76.0445	(2)
76.034	(10)	O V	76.1128	(2)
76.034	(10)	O V	76.2003	(5)
76.513	(9)	Fe V	76.5177	(2)
76.513	(9)	N IV	76.5148	(2)
77.448	(10)	O V	77.4518	(2)
77.984	(13)	O IV	77.9734	(2)
77.984	(13)	O IV	77.9821	(5)
77.984	(13)	O IV	77.9912	(2)
77.984	(13)	O IV	77.9997	(2)
83.435	(10)	O III	83.2927	(2)
83.435	(10)	O III	83.3742	(5)
83.435	(10)	O III	83.5096	(2)
83.435	(10)	O III	83.5292	(2)
83.903	(10)	Fe III	83.8937	(2)
83.903	(10)	Fe III	83.9001	(0.7)

83.903	(10)	Fe III	83.8869	(1.1)
86.875	(11)	Fe III	86.8837	(2)
86.875	(11)	Fe III	86.8434	(0.15)
86.875	(11)	Fe III	86.8477	(0.2)
88.311	(9)	Fe III	88.3091	(5)
88.311	(9)	Fe III	88.3091	(1.1)
88.311	(9)	Fe III	88.3689	(10)
89.078	(9)	Fe III	89.0754	(5)
90.405	(9)	Fe V	90.4109	(5)
91.642	(10)	Fe III	91.6522	(5)
91.642	(10)	Fe III	91.6148	(5)
91.642	(10)	Fe III	91.6522	(10)
91.642	(10)	Fe V	91.6960	(10)
91.910	(10)	Fe III	91.8781	(5)
91.910	(10)	Fe III	91.9167	(5)
92.313	(9)	Fe V	92.2891	(5)
92.313	(9)	Fe V	92.3039	(5)
92.313	(9)	Fe V	92.2689	(10)
92.313	(9)	Fe V	92.2295	(10)
92.313	(9)	Fe V	92.1778	(10)
92.313	(9)	Fe V	92.1836	(10)
92.313	(9)	Fe V	92.3728	(10)
92.313	(9)	Fe V	92.3984	(10)
92.313	(9)	Fe V	92.4039	(10)
92.313	(9)	Fe III	92.3963	(5)
92.313	(9)	Fe V	92.4320	(10)
92.313	(9)	Fe V	92.4668	(10)
93.168	(10)	Fe V	93.0724	(10)
93.168	(10)	Fe V	93.1259	(10)
93.168	(10)	Fe V	93.1461	(5)
93.168	(10)	Fe V	93.1980	(10)
93.168	(10)	Fe V	93.2547	(10)
97.701	(9)	Fe V	97.6534	(5)
97.701	(9)	Fe V	97.6849	(5)
97.701	(9)	Fe V	97.7210	(5)
97.701	(9)	Fe V	97.7431	(5)

97.701	(9)	C III	97.7030	(5)
98.977	(10)	Fe V	98.9257	(5)
98.977	(10)	Fe V	98.9427	(5)
98.977	(10)	Fe V	98.9871	(5)
98.977	(10)	Fe V	98.9926	(10)
98.977	(10)	Fe V	98.9949	(10)
98.977	(10)	Fe V	99.0296	(5)
99.152	(10)	Fe V	99.1128	(5)
99.152	(10)	Fe V	99.1574	(5)
99.152	(10)	Fe V	99.1708	(5)
99.152	(10)	Fe V	99.1950	(5)
99.152	(10)	Fe V	99.2185	(5)
99.152	(10)	Fe V	99.2268	(5)
101.621	(10)	Fe V	101.5516	(5)
101.621	(10)	Fe V	101.5709	(5)
101.621	(10)	Fe V	101.6062	(5)
101.621	(10)	Fe V	101.6188	(5)
101.621	(10)	Fe V	101.6288	(5)
101.621	(10)	Fe V	101.6974	(10)
102.110	(10)	Fe V	102.1176	(10)
102.110	(10)	Fe V	102.1123	(10)
102.110	(10)	Fe V	102.1011	(5)
102.110	(10)	Fe III	102.1646	(10)
107.043	(9)	Fe V	107.0379	(5)
110.879	(9)	O IV	55.4075	(10)
110.879	(9)	O IV	55.4514	(10)
114.860	(13)	C III	57.4281	(5)
114.860	(13)	Fe II	114.8947	(5)
117.561	(9)	C III	117.4930	(5)
117.561	(9)	C III	117.5260	(5)
117.561	(9)	C III	117.5590	(5)
117.561	(9)	C III	117.5710	(5)
117.561	(9)	C III	117.5990	(5)
117.561	(9)	C III	117.6370	(5)
119.913	(11)	Fe V	119.8593	(5)
119.913	(11)	Fe II	119.8660	(5)

119.913	(11)	Fe II	119.8924	(5)
119.913	(11)	Fe II	119.9681	(5)
119.913	(11)	Fe II	119.9821	(5)
121.562	(10)	Fe III	121.5244	(10)
121.822	(9)	Fe V	121.7993	(10)
123.875	(9)	N V	123.8821	(5)
124.275	(9)	N V	124.2804	(5)
127.759	(13)	C I	127.7517	(5)
127.759	(13)	C I	127.7285	(5)
127.759	(13)	C I	127.7250	(5)
127.759	(13)	C I	127.7556	(5)
133.506	(14)	Fe III	133.5149	(5)
133.506	(14)	Fe II	133.4822	(10)
133.506	(14)	Fe II	133.4522	(10)
133.506	(14)	Fe II	133.5268	(5)
133.506	(14)	Fe II	133.5409	(10)
133.506	(14)	Fe II	133.5834	(5)
133.506	(14)	Fe II	133.5861	(10)
137.138	(12)	O V	137.1292	(10)
137.866	(13)	Fe V	137.8560	(10)
137.866	(13)	Fe V	137.8092	(5)
137.866	(13)	Fe V	137.9206	(5)
139.584	(10)	Fe V	139.5442	(5)
139.780	(9)	Fe V	139.7753	(10)
153.006	(9)	N IV	2x76.5148	(10)
153.006	(9)	Fe V	2x76.5177	(5)
157.519	(11)	O IV	2x78.7711	(5)
160.539	(9)	Fe II	160.5324	(5)
160.539	(9)	Fe II	160.5418	(5)
165.978	(11)	Fe II	165.9483	(5)
166.311	(10)	Fe II	166.3223	(5)
176.583	(9)	Fe III	2x88.3091	(5)
176.583	(9)	Fe III	2x88.3689	(5)
176.583	(9)	Fe III	2x88.3412	(10)
178.130	(10)	Fe III	2x89.0754	(10)
180.782	(11)	Fe V	2x90.4109	(5)

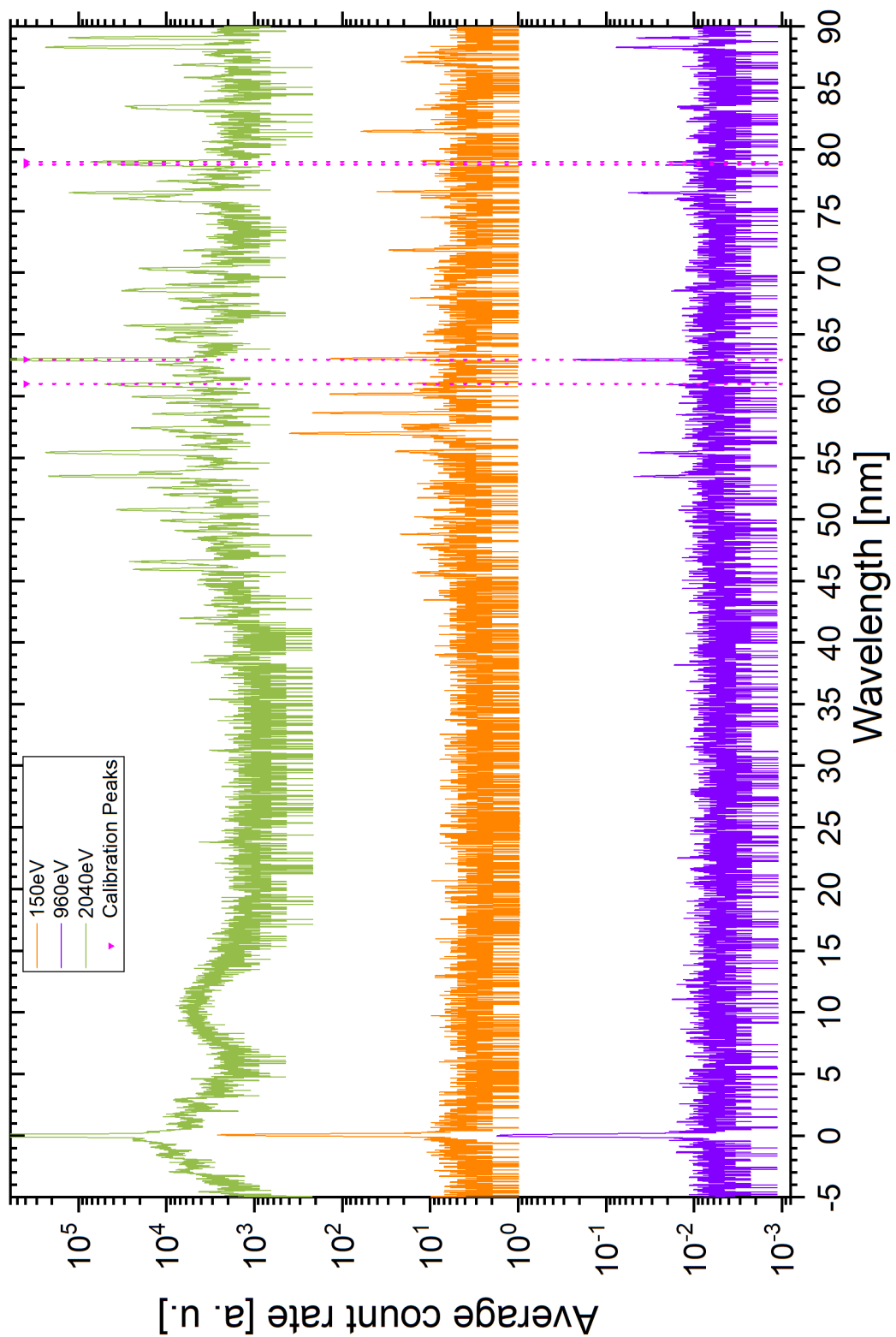


Figure 5.6.: This graph shows three spectra, acquired at three different electron beam energies, indicated by different colors. The oxygen calibration lines are depicted as pink dotted lines. The wavelength regime is -5nm to 90nm

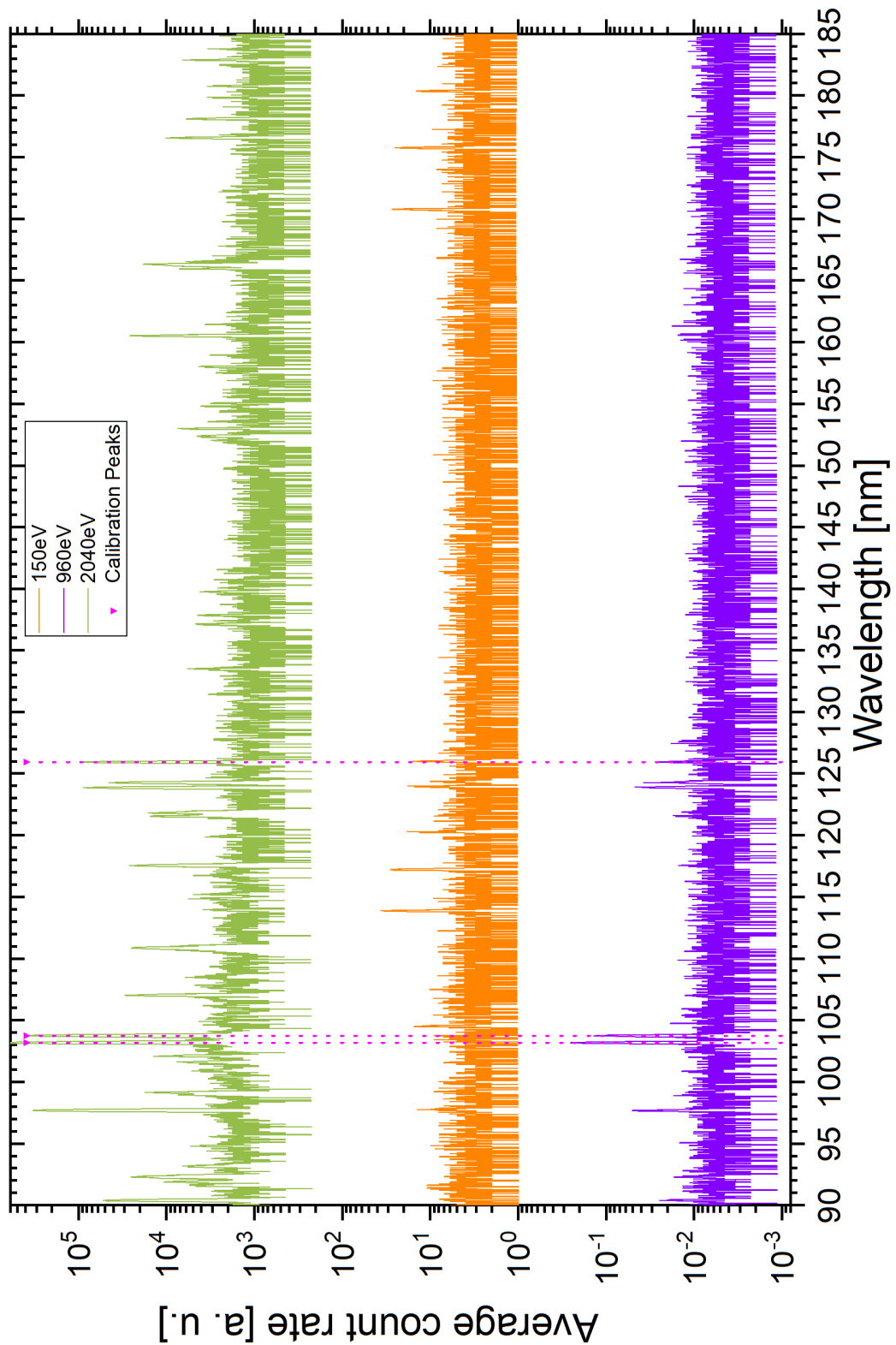


Figure 5.7.: This graph shows three spectra, acquired at three different electron beam energies, which is indicated by different colors. The oxygen calibration lines are depicted as pink dotted lines. The covered wavelength regime is 90nm to 180nm.

6. Summary and outlook

The primary aim of this thesis was to observe and identify spectral ionic iron – especially of the charge state Fe V – in the EUV and VUV regime. Since data of Fe spectra, observed in white dwarfs was used to calculate a variation of the fine structure constant hinting on Physics beyond the Standard Model, these lines are of particular interest.

In order to operate spectroscopy on these ions, the FLASH EBIT at the Max-Planck Institut für Kernphysik was used. This instrument is equipped with two spectrometers, for the EUV and the VUV regime. The 3m VUV grating spectrometer utilizes the ORFEUS detector and had to be optimized first to maximize the line resolution.

For spectra measurements, the incidence grating had to be rotated in order to acquire a wide-range spectrum, therefore the detector was positioned on a linear stage to move into the right position. To automate this process, a program which calculates the respective motor position for a given incidence angle and moves the detector to this position was presented. For the calculation of the focus positions, an interpolation of manually determined focuses at different angles was implemented into the program.

This interpolation could be further optimised by determining the focus position of even more lines. Due to a longer integration time per measurement at a fixed angle, the line width at this fixed angle could be determined more accurately, leading to an increased resolution.

After optimization of the detector, several measurements of wide-range iron spectra at different energies were performed. Since the acquired data was in terms of the incidence grating angle, a calibration was needed to translate the angles into wavelengths. For the calibration several oxygen lines were identified and utilised, and a cubic function was chosen for the interpolation of the dispersive relation.

A spectrum at an electron beam energy of 2040 eV was measured and analyzed, and a total number of around 450 lines could be identified. Among others, several lines of oxygen and carbon for the charge states O III – O V and C III-IV were matched and documented. Further, iron lines of the charge states Fe II, Fe III and Fe V were identified, even though the identification is questionable for the given electron beam energy. For

this energy, helium-like and lithium-like iron lines were expected in 2nd-order, but could not be determined in the spectrum.

To challenge the hypothesis on the identified of Fe V lines, more measurements at different electron beam energies should be performed. The ionization energy of Fe V lies at around 72.9 eV, therefore measurements at electron beam energies in this regime are advised. Since the FLASH EBIT tends to be unstable at low electron beam energies due to the high distance the electron beam has to travel, this measurements could also be performed with Heidelberg's compact Mini-EBITs.

Bibliography

- [1] O. Neugebauer, *Publications of the Astronomical Society of the Pacific* **58**, 17 (1946), ISSN 00046280, 15383873, URL <http://www.jstor.org/stable/40671862>.
- [2] I. Newton, *Philosophical Transactions of the Royal Society of London* **6**, 3075 (1672), URL <https://royalsocietypublishing.org/doi/abs/10.1098/rstl.1671.0072>.
- [3] W. H. Wollaston, *Philosophical Transactions of the Royal Society of London* **92**, 365 (1802), URL <https://royalsocietypublishing.org/doi/abs/10.1098/rstl.1802.0014>.
- [4] J. Fraunhofer, *Annalen der Physik* **56**, 264 (1817), <https://onlinelibrary.wiley.com/doi/pdf/10.1002/andp.18170560706>, URL <https://onlinelibrary.wiley.com/doi/abs/10.1002/andp.18170560706>.
- [5] G. Kirchhoff and R. Bunsen, *Annalen der Physik* **189**, 337 (1861), URL <https://onlinelibrary.wiley.com/doi/abs/10.1002/andp.18611890702>.
- [6] J. Barnstedt, N. Kappelmann, I. Appenzeller, A. Fromm, M. Gölz, M. Grewing, W. Gringel, C. Haas, W. Hopfensitz, G. Krämer, et al., *Astron. Astrophys. Suppl. Ser.* **134**, 561 (1999), URL <https://doi.org/10.1051/aas:1999156>.
- [7] J. Barnstedt, W. Gringel, N. Kappelmann, and M. Grewing, *Astron. Astrophys. Suppl. Ser.* **143**, 193 (2000), URL <https://doi.org/10.1051/aas:2000176>.
- [8] V. S. Aguirre (Springer International Publishing, 2018), pp. 3–25, ISBN 978-3-319-59315-9.
- [9] B. Zuckerman, D. Koester, I. N. Reid, and M. Hunsch, *The Astrophysical Journal* **596**, 477 (2003), URL <https://doi.org/10.1086/377492>.
- [10] E. L. Schatzman, *White dwarfs* (1958).

- [11] J. C. Berengut, V. V. Flambaum, A. Ong, J. K. Webb, J. D. Barrow, M. A. Barstow, S. P. Preval, and J. B. Holberg, *Phys. Rev. Lett.* **111**, 10801 (2013).
- [12] F. Torretti, A. Windberger, A. Ryabtsev, S. Dobrodey, H. Bekker, W. Ubachs, R. Hoekstra, E. V. Kahl, J. C. Berengut, J. R. C. López-Urrutia, et al., *Phys. Rev. A* **95**, 42503 (2017), URL <https://link.aps.org/doi/10.1103/PhysRevA.95.042503>.
- [13] W. Demtroder, *Atoms, molecules and photons : an introduction to atomic-, molecular-, and quantum-physics* (Springer, 2010), ISBN 9783642102974.
- [14] E. Schrödinger, *Annalen der Physik* **385**, 437 (1926), URL <https://onlinelibrary.wiley.com/doi/abs/10.1002/andp.19263851302>.
- [15] R. K. Nesbet and D. R. Hartree, *Proceedings of the Royal Society of London. Series A. Mathematical and Physical Sciences* **230**, 312 (1955), URL <https://royalsocietypublishing.org/doi/abs/10.1098/rspa.1955.0134>.
- [16] S. Dobrodey, Ph.D. thesis (2019).
- [17] M. A. Levine, R. E. Marrs, J. R. Henderson, D. A. Knapp, and M. B. Schneider, *Physica Scripta* **1988** (1988), ISSN 14024896.
- [18] D. Richter, *Mechanics of gases* (2010).
- [19] J. R. C. Lopez-Urrutia and Z. Harman, *Springer Tracts Mod. Phys.* **256**, 315 (2014).
- [20] W. Lotz, *Zeitschrift für Physik* **216**, 241 (1968), ISSN 0044-3328, URL <https://doi.org/10.1007/BF01392963>.
- [21] H. van Regemorter, **136**, 906 (1962).
- [22] Y. S. Kim and R. H. Pratt, *Phys. Rev. A* **27**, 2913 (1983), URL <https://link.aps.org/doi/10.1103/PhysRevA.27.2913>.
- [23] S. W. Epp, Ph.D. thesis (2007).
- [24] G. Herrmann, *Journal of Applied Physics* **29**, 127 (1958), URL <https://doi.org/10.1063/1.1723053>.
- [25] M. W. Wolfmeyer and J. R. Dillinger, *Physics Letters A* **34** (1971), ISSN 03759601.
- [26] M. A. Blessenohl, Ph.D. thesis (2020).

- [27] H. A. Rowland, The London, Edinburgh, and Dublin Philosophical Magazine and Journal of Science **16**, 197 (1883), URL <https://doi.org/10.1080/14786448308627419>.
- [28] G. Reichardt, T. Noll, I. Packe, P. Rotter, J.-S. Schmidt, and W. Gudat, Nuclear Instruments and Methods in Physics Research Section A: Accelerators, Spectrometers, Detectors and Associated Equipment **467-468**, 458 (2001), ISSN 0168-9002, 7th Int.Conf. on Synchrotron Radiation Instrumentation, URL <https://www.sciencedirect.com/science/article/pii/S0168900201003576>.
- [29] T. Harada and T. Kita, Appl. Opt. **19**, 3987 (1980), URL <http://ao.osa.org/abstract.cfm?URI=ao-19-23-3987>.
- [30] T. Baumann, Ph.D. thesis (2012).
- [31] S. Dobrodey, *Untersuchung von K-LL-Resonanzen dielektronischer Rekombination und simultaner Innerschalen-Vakuum-Ultraviolett Übergänge in hochgeladenem Eisen mit einer Elektronenstrahl-Ionenfalle* (2014).
- [32] *Nist standard reference database 78*, <https://www.nist.gov/pml/atomic-spectra-database>.

A. Appendix

In the following, a list of the identified lines in the 2040eV spectrum is provided. The listed data was acquired from NIST.

Table A.1.: A list of all the identified lines in the spectrum at 2040eV

Charge state	λ [nm]	$\Delta\lambda_{\text{NIST}}$ [nm]
C III	37.1690	(10)
C III	37.1750	(10)
C III	37.1780	(10)
C III	38.6203	(10)
C III	45.0734	(10)
C III	45.9460	(10)
C III	45.9520	(10)
C III	45.9520	(10)
C III	45.9630	(10)
C III	51.1522	(10)
C III	53.5288	(10)
C III	53.8080	(10)
C III	53.8149	(10)
C III	53.8312	(10)
C III	57.4281	(10)
C III	97.7030	(10)
C III	117.4930	(10)
C III	117.5260	(10)
C III	117.5590	(10)
C III	117.5710	(10)
C III	117.5990	(10)
C III	117.6370	(10)
C III	38.9090	(10)
C III	93.3735	(10)
C III	38.9005	(10)
C III	38.8969	(10)
C III	56.6482	(10)
C III	58.5662	(10)
C III	58.5499	(10)
C III	58.5610	(10)
C III	69.0521	(10)
C III	124.6721	(10)
C IV	31.2420	(100)

C IV	31.2460	(100)
C IV	38.4030	(100)
C IV	38.4180	(100)
C IV	41.9710	(100)
C IV	41.9520	(100)
C IV	123.0521	(100)
Fe II	109.3056	(2)
Fe II	111.0815	(2)
Fe II	113.2990	(5)
Fe II	114.4926	(2)
Fe II	114.4926	(2)
Fe II	114.5508	(2)
Fe II	114.5508	(2)
Fe II	114.8947	(2)
Fe II	114.8947	(2)
Fe II	116.9163	(2)
Fe II	118.3033	(2)
Fe II	119.8660	(2)
Fe II	119.8924	(2)
Fe II	119.9231	(2)
Fe II	119.9539	(2)
Fe II	119.9681	(5)
Fe II	119.9821	(2)
Fe II	119.9821	(2)
Fe II	125.1413	(2)
Fe II	125.1254	(2)
Fe II	133.4822	(5)
Fe II	133.4522	(2)
Fe II	133.5268	(2)
Fe II	133.5409	(2)
Fe II	133.5834	(5)
Fe II	133.5861	(2)
Fe II	134.2141	(2)
Fe II	134.6826	(2)
Fe II	160.5218	(0.7)
Fe II	160.5324	(1.1)

Fe II	160.5418	(2)
Fe II	165.9483	(0.15)
Fe II	166.3223	(0.2)
Fe II	167.7837	(5)
Fe II	160.5324	(1.1)
Fe III	69.9464	(10)
Fe III	70.0130	(5)
Fe III	70.0571	(5)
Fe III	70.1024	(5)
Fe III	70.1353	(5)
Fe III	70.7434	(10)
Fe III	70.7434	(10)
Fe III	70.7808	(5)
Fe III	85.8550	(5)
Fe III	85.8604	(5)
Fe III	85.9084	(5)
Fe III	85.9726	(10)
Fe III	85.9726	(10)
Fe III	85.9745	(10)
Fe III	85.9833	(10)
Fe III	85.9833	(10)
Fe III	86.8837	(10)
Fe III	86.8837	(10)
Fe III	86.8434	(5)
Fe III	86.8477	(10)
Fe III	86.8477	(10)
Fe III	88.3091	(10)
Fe III	88.3091	(10)
Fe III	88.3689	(5)
Fe III	88.3400	(10)
Fe III	88.3400	(10)
Fe III	89.0754	(5)
Fe III	89.3105	(5)
Fe III	89.4008	(5)
Fe III	89.4378	(5)
Fe III	89.5841	(5)

Fe III	89.7409	(5)
Fe III	89.8806	(5)
Fe III	90.5958	(5)
Fe III	90.7040	(10)
Fe III	90.7040	(10)
Fe III	90.7890	(5)
Fe III	91.0686	(5)
Fe III	91.1263	(5)
Fe III	91.1200	(5)
Fe III	91.1952	(5)
Fe III	91.2193	(5)
Fe III	91.2340	(5)
Fe III	91.2449	(5)
Fe III	91.2684	(5)
Fe III	91.2788	(5)
Fe III	91.3130	(5)
Fe III	91.4012	(5)
Fe III	91.5603	(10)
Fe III	91.5603	(10)
Fe III	91.6522	(10)
Fe III	91.6148	(5)
Fe III	91.6522	(10)
Fe III	91.8781	(5)
Fe III	91.9167	(10)
Fe III	91.9167	(10)
Fe III	92.3963	(5)
Fe III	92.6632	(5)
Fe III	92.6706	(5)
Fe III	92.7265	(5)
Fe III	92.7999	(5)
Fe III	92.8638	(5)
Fe III	92.9630	(5)
Fe III	93.4693	(5)
Fe III	93.7458	(5)
Fe III	93.7578	(5)
Fe III	94.2674	(5)

Fe III	94.2698	(5)
Fe III	94.2790	(5)
Fe III	95.0328	(5)
Fe III	95.0724	(5)
Fe III	96.3083	(10)
Fe III	96.3083	(10)
Fe III	97.3499	(5)
Fe III	98.8246	(5)
Fe III	102.1646	(5)
Fe III	106.2031	(5)
Fe III	106.8288	(5)
Fe III	106.8190	(5)
Fe III	67.9124	(5)
Fe III	68.5454	(10)
Fe III	68.5454	(10)
Fe III	83.8937	(5)
Fe III	83.9001	(10)
Fe III	83.8869	(5)
Fe III	83.9001	(10)
Fe III	84.0145	(10)
Fe III	84.0145	(10)
Fe III	84.7400	(5)
Fe III	85.1330	(5)
Fe III	85.1149	(5)
Fe III	108.5449	(10)
Fe III	108.5449	(10)
Fe III	108.4542	(5)
Fe III	108.4131	(5)
Fe III	108.4585	(5)
Fe III	108.4644	(5)
Fe III	112.2533	(5)
Fe III	116.1875	(5)
Fe III	121.5244	(5)
Fe III	128.4233	(5)
Fe III	128.6647	(5)
Fe III	128.7757	(10)

Fe III	128.7757	(10)
Fe III	133.5149	(5)
Fe III	134.4041	(5)
Fe III	156.1179	(15)
Fe III	156.1179	(15)
Fe III	156.8820	(15)
Fe III	156.9070	(30)
Fe III	161.4639	(10)
Fe III	161.4639	(10)
Fe V	71.1638	(6)
Fe V	43.4418	(5)
Fe V	85.8696	(6)
Fe V	85.8199	(6)
Fe V	86.0172	(6)
Fe V	89.4458	(6)
Fe V	89.4548	(6)
Fe V	91.6960	(6)
Fe V	92.2891	(6)
Fe V	92.3039	(6)
Fe V	92.2689	(6)
Fe V	92.2295	(6)
Fe V	92.1778	(6)
Fe V	92.1836	(6)
Fe V	92.3728	(6)
Fe V	92.3984	(6)
Fe V	92.4039	(6)
Fe V	92.4320	(6)
Fe V	92.4668	(6)
Fe V	92.6678	(6)
Fe V	92.6873	(6)
Fe V	92.8189	(6)
Fe V	92.8087	(6)
Fe V	92.8087	(6)
Fe V	92.8189	(6)
Fe V	92.9071	(6)
Fe V	92.8972	(6)

Fe V	92.9339	(6)
Fe V	93.0724	(6)
Fe V	93.1259	(6)
Fe V	93.1461	(6)
Fe V	93.1980	(6)
Fe V	93.2547	(6)
Fe V	93.4792	(6)
Fe V	93.7933	(6)
Fe V	93.8001	(6)
Fe V	93.8060	(6)
Fe V	93.8283	(12)
Fe V	93.8283	(12)
Fe V	93.8817	(6)
Fe V	93.8740	(6)
Fe V	93.8657	(6)
Fe V	94.0019	(6)
Fe V	94.0176	(6)
Fe V	94.0285	(6)
Fe V	94.1740	(6)
Fe V	94.1631	(12)
Fe V	94.1335	(6)
Fe V	94.1485	(6)
Fe V	94.1573	(6)
Fe V	94.2649	(6)
Fe V	94.3754	(12)
Fe V	94.3754	(12)
Fe V	94.5027	(12)
Fe V	94.5265	(6)
Fe V	94.6054	(6)
Fe V	94.6196	(6)
Fe V	94.6902	(6)
Fe V	94.7382	(6)
Fe V	94.8039	(6)
Fe V	94.8786	(6)
Fe V	94.8591	(6)
Fe V	94.8912	(6)

Fe V	95.1283	(6)
Fe V	95.2052	(6)
Fe V	95.2382	(6)
Fe V	95.4447	(6)
Fe V	95.4866	(6)
Fe V	95.5736	(6)
Fe V	95.6310	(6)
Fe V	95.6508	(6)
Fe V	95.6677	(6)
Fe V	95.7908	(6)
Fe V	95.9079	(12)
Fe V	96.0141	(6)
Fe V	96.1968	(6)
Fe V	96.4950	(6)
Fe V	96.4710	(6)
Fe V	96.6045	(12)
Fe V	96.6045	(12)
Fe V	96.6324	(12)
Fe V	96.6324	(12)
Fe V	96.6590	(12)
Fe V	96.6590	(12)
Fe V	96.7233	(6)
Fe V	96.7516	(6)
Fe V	96.7869	(6)
Fe V	97.0621	(6)
Fe V	97.1246	(6)
Fe V	97.1564	(12)
Fe V	97.1564	(12)
Fe V	97.1952	(6)
Fe V	97.2204	(6)
Fe V	97.3196	(6)
Fe V	97.3141	(6)
Fe V	97.4152	(6)
Fe V	97.4952	(6)
Fe V	97.6534	(6)
Fe V	97.6849	(6)

Fe V	97.7210	(12)
Fe V	97.7210	(12)
Fe V	97.7431	(6)
Fe V	97.7979	(6)
Fe V	97.8037	(6)
Fe V	97.8106	(6)
Fe V	97.8200	(6)
Fe V	97.8837	(6)
Fe V	97.9556	(6)
Fe V	98.0132	(6)
Fe V	98.0187	(12)
Fe V	98.0187	(12)
Fe V	98.0813	(6)
Fe V	98.0850	(6)
Fe V	98.1892	(6)
Fe V	98.2210	(6)
Fe V	98.2639	(6)
Fe V	98.3990	(12)
Fe V	98.4051	(12)
Fe V	98.4183	(6)
Fe V	98.4407	(6)
Fe V	98.5126	(6)
Fe V	98.6091	(12)
Fe V	98.6091	(12)
Fe V	98.6261	(6)
Fe V	98.6912	(6)
Fe V	98.7061	(6)
Fe V	98.9257	(6)
Fe V	98.9427	(6)
Fe V	98.9871	(6)
Fe V	98.9926	(6)
Fe V	98.9949	(6)
Fe V	99.0296	(6)
Fe V	99.0852	(6)
Fe V	99.1128	(6)
Fe V	99.1574	(6)

Fe V	99.1708	(6)
Fe V	99.1950	(6)
Fe V	99.2185	(6)
Fe V	99.2268	(12)
Fe V	99.2268	(12)
Fe V	99.2711	(6)
Fe V	99.2758	(6)
Fe V	99.3079	(12)
Fe V	99.4460	(6)
Fe V	99.5261	(6)
Fe V	99.5360	(12)
Fe V	99.5360	(12)
Fe V	99.5430	(12)
Fe V	99.6828	(6)
Fe V	99.6949	(6)
Fe V	99.7115	(6)
Fe V	99.9033	(6)
Fe V	99.9629	(12)
Fe V	99.9629	(12)
Fe V	99.9629	(12)
Fe V	100.0769	(6)
Fe V	100.1451	(6)
Fe V	100.1558	(6)
Fe V	100.3697	(6)
Fe V	100.5962	(6)
Fe V	101.2867	(6)
Fe V	101.2822	(6)
Fe V	101.3198	(6)
Fe V	101.4437	(6)
Fe V	101.5516	(6)
Fe V	101.5709	(6)
Fe V	101.6062	(6)
Fe V	101.6188	(12)
Fe V	101.6288	(6)
Fe V	101.6974	(6)
Fe V	102.1176	(6)

Fe V	102.1123	(6)
Fe V	102.1011	(6)
Fe V	102.2051	(6)
Fe V	102.2422	(6)
Fe V	102.2473	(6)
Fe V	102.2531	(6)
Fe V	102.5232	(6)
Fe V	102.5544	(6)
Fe V	102.6364	(12)
Fe V	102.8873	(12)
Fe V	102.8873	(12)
Fe V	103.4975	(6)
Fe V	104.6323	(6)
Fe V	105.0920	(6)
Fe V	105.3966	(6)
Fe V	105.4059	(6)
Fe V	105.8358	(6)
Fe V	107.0379	(6)
Fe V	107.6969	(6)
Fe V	107.5575	(12)
Fe V	90.4109	(6)
Fe V	90.4109	(6)
Fe V	38.9390	(3)
Fe V	38.9339	(3)
Fe V	38.9115	(3)
Fe V	38.9146	(3)
Fe V	38.9161	(3)
Fe V	38.7984	(3)
Fe V	38.8030	(3)
Fe V	38.8134	(5)
Fe V	38.8134	(5)
Fe V	38.8199	(3)
Fe V	39.2290	(3)
Fe V	39.2352	(3)
Fe V	39.2381	(3)
Fe V	39.2503	(3)

Fe V	39.2702	(5)
Fe V	39.2702	(5)
Fe V	39.2770	(3)
Fe V	39.2910	(3)
Fe V	41.5013	(3)
Fe V	41.5834	(5)
Fe V	41.5834	(5)
Fe V	42.6056	(3)
Fe V	42.6108	(3)
Fe V	42.8752	(3)
Fe V	43.4418	(5)
Fe V	43.4418	(5)
Fe V	43.4658	(3)
Fe V	43.4686	(3)
Fe V	43.3872	(3)
Fe V	76.5177	(6)
Fe V	74.8146	(6)
Fe V	71.7906	(6)
Fe V	71.7954	(6)
Fe V	71.8659	(6)
Fe V	73.6407	(12)
Fe V	73.9351	(6)
Fe V	73.9511	(6)
Fe V	76.8028	(6)
Fe V	82.1378	(6)
Fe V	84.1812	(6)
Fe V	114.5243	(6)
Fe V	119.8593	(4)
Fe V	121.7993	(4)
Fe V	124.9496	(4)
Fe V	133.6039	(4)
Fe V	134.3121	(7)
Fe V	135.1755	(4)
Fe V	137.8560	(4)
Fe V	137.8092	(4)
Fe V	137.9206	(4)

Fe V	139.7753	(4)
Fe V	139.5442	(4)
O III	50.7683	(25)
O III	50.8182	(25)
O III	52.5795	(25)
O III	59.7818	(25)
O III	59.9598	(25)
O III	61.0040	(25)
O III	61.0750	(25)
O III	61.0850	(25)
O III	70.2332	(25)
O III	70.2822	(25)
O III	70.2899	(25)
O III	70.2899	(25)
O III	70.3850	(25)
O III	70.3850	(25)
O III	83.2927	(25)
O III	83.3742	(25)
O III	83.5096	(25)
O III	83.5292	(25)
O III	52.5795	(25)
O III	158.9913	(25)
O III	166.5799	(25)
O V	62.9730	(25)
O V	75.8678	(25)
O V	75.9441	(25)
O V	76.0228	(25)
O V	76.0445	(25)
O V	76.1128	(25)
O V	76.2003	(25)
O V	77.4518	(25)
O V	137.1292	(25)

Erklärung

Ich versichere, dass ich diese Arbeit selbstständig verfasst und keine anderen als die angegebenen Quellen und Hilfsmittel benutzt habe.

Heidelberg, den ...*27.08.2021*,

A handwritten signature in blue ink, appearing to read "A. Seitzewski". The signature is stylized and cursive.